Planck intermediate results

XLIV. Structure of the Galactic magnetic field from dust polarization maps of the southern Galactic cap

Planck Collaboration: N. Aghanim[51], M. I. R. Alves[82,9,51], D. Arzoumanian[51,64], J. Aumont[51], C. Baccigalupi[74], M. Ballardini[26,42,45], A. J. Banday[82,9], R. B. Barreiro[56], N. Bartolo[25,57], S. Basak[74], K. Benabed[52,81], J.-P. Bernard[82,9], M. Bersanelli[29,43], P. Bielewicz[71,9,74], L. Bonavera[56], J. R. Bond[8], J. Borrill[11,78], F. R. Bouchet[52,77], F. Boulanger[51], A. Bracco[51,64 ★], M. Bucher[1], C. Burigana[42,27,45], E. Calabrese[79], J.-F. Cardoso[65,1,52], H. C. Chiang[22,7], L. P. L. Colombo[19,58], C. Combet[66], B. Comis[66], F. Couchot[62], A. Coulais[63], B. P. Crill[58,10], A. Curto[56,6,61], F. Cuttaia[42], R. J. Davis[59], P. de Bernardis[28], A. de Rosa[42], G. de Zotti[39,74], J. Delabrouille[1], J.-M. Delouis[52,81], E. Di Valentino[52,77], C. Dickinson[59], J. M. Diego[56], O. Doré[58,10], M. Douspis[51], A. Ducout[52,50], X. Dupac[33], S. Dusini[57], G. Efstathiou[53], F. Elsner[20,52,81], T. A. Enßlin[69], H. K. Eriksen[54], E. Falgarone[63], Y. Fantaye[31], K. Ferrière[82,9], F. Finelli[42,45], M. Frailis[41], A. A. Fraisse[22], E. Franceschi[42], A. Frolov[76], S. Galeotta[41], S. Galli[60], K. Ganga[1], R. T. Génova-Santos[55,15], M. Gerbino[80,73,28], T. Ghosh[51], J. González-Nuevo[16,56], K. M. Górski[58,84], S. Gratton[61,53], A. Gregorio[30,41,49], A. Gruppuso[42], J. E. Gudmundsson[80,73,22], V. Guillet[51], F. K. Hansen[54], G. Helou[10], S. Henrot-Versillé[62], D. Herranz[56], E. Hivon[52,81], Z. Huang[8], A. H. Jaffe[50], T. R. Jaffe[82,9], W. C. Jones[22], E. Keihänen[21], R. Keskitalo[11], T. S. Kisner[68], N. Krachmalnicoff[29], M. Kunz[14,51,3], H. Kurki-Suonio[21,38], G. Lagache[5,51], A. Lähteenmäki[2,38], J.-M. Lamarre[63], M. Langer[51], A. Lasenby[6,61], M. Lattanzi[27,46], M. Le Jeune[1], F. Levrier[63], M. Liguori[25,57], P. B. Lilje[54], M. López-Caniego[33,56], P. M. Lubin[23], J. F. Macías-Pérez[66], G. Maggio[41], D. Maino[29,43], N. Mandolesi[42,27], A. Mangilli[51,62], M. Maris[41], P. G. Martin[8], E. Martínez-González[56], S. Matarrese[25,57,35], N. Mauri[45], J. D. McEwen[70], A. Melchiorri[28,47], A. Mennella[29,43], M. Migliaccio[53,61], M.-A. Miville-Deschênes[51,8], D. Molinari[27,42,46], A. Moneti[52], L. Montier[82,9], G. Morgante[42], A. Moss[75], P. Naselsky[72,32], P. Natoli[27,4,46], J. Neveu[63,62], H. U. Nørgaard-Nielsen[13], N. Oppermann[8], C. A. Oxborrow[13], L. Pagano[28,47], D. Paoletti[42,45], B. Partridge[37], O. Perdereau[62], L. Perotto[66], V. Pettorino[36], F. Piacentini[28], S. Plaszczynski[62], G. Polenta[4,40], J. P. Rachen[17,69], R. Rebolo[55,12,15], M. Reinecke[69], M. Remazeilles[59,51,1], A. Renzi[31,48], I. Ristorcelli[82,9], G. Rocha[58,10], M. Rossetti[29,43], G. Roudier[1,63,58], B. Ruiz-Granados[83], L. Salvati[28], M. Sandri[42], M. Savelainen[21,38], D. Scott[18], C. Sirignano[25,57], J. D. Soler[51,64], A.-S. Suur-Uski[21,38], J. A. Tauber[34], D. Tavagnacco[41,30], M. Tenti[44], L. Toffolatti[16,56,42], M. Tomasi[29,43], M. Tristram[62], T. Trombetti[42,27], J. Valiviita[21,38], F. Vansyngel[51], F. Van Tent[67], P. Vielva[56], F. Villa[42], B. D. Wandelt[52,81,24], I. K. Wehus[58,54], A. Zacchei[41], and A. Zonca[23]

(Affiliations can be found after the references)

ABSTRACT

Using data from the *Planck* satellite, we study the statistical properties of interstellar dust polarization at high Galactic latitudes around the south pole ($b < -60°$). Our aim is to advance the understanding of the magnetized interstellar medium (ISM), and to provide a modelling framework of the polarized dust foreground for use in cosmic microwave background (CMB) component-separation procedures. We examine the Stokes I, Q, and U maps at 353 GHz, and particularly the statistical distribution of the polarization fraction (p) and angle (ψ), in order to characterize the ordered and turbulent components of the Galactic magnetic field (GMF) in the solar neighbourhood. The Q and U maps show patterns at large angular scales, which we relate to the mean orientation of the GMF towards Galactic coordinates $(l_0, b_0) = (70° \pm 5°, 24° \pm 5°)$. The histogram of the observed p values shows a wide dispersion up to 25%. The histogram of ψ has a standard deviation of 12° about the regular pattern expected from the ordered GMF. We build a phenomenological model that connects the distributions of p and ψ to a statistical description of the turbulent component of the GMF, assuming a uniform effective polarization fraction (p_0) of dust emission. To compute the Stokes parameters, we approximate the integration along the line of sight (LOS) as a sum over a set of N independent polarization layers, in each of which the turbulent component of the GMF is obtained from Gaussian realizations of a power-law power spectrum. We are able to reproduce the observed p and ψ distributions using a p_0 value of 26%, a ratio of 0.9 between the strengths of the turbulent and mean components of the GMF, and a small value of N. The mean value of p (inferred from the fit of the large-scale patterns in the Stokes maps) is $12 \pm 1\%$. We relate the polarization layers to the density structure and to the correlation length of the GMF along the LOS. We emphasize the simplicity of our model (involving only a few parameters), which can be easily computed on the celestial sphere to produce simulated maps of dust polarization. Our work is an important step towards a model that can be used to assess the accuracy of component-separation methods in present and future CMB experiments designed to search the B mode CMB polarization from primordial gravity waves.

Key words. magnetohydrodynamics (MHD) – polarization – methods: data analysis – dust, extinction – cosmic background radiation – ISM: magnetic fields

1. Introduction

Interstellar magnetic fields are tied to the interstellar gas. Together with cosmic rays they form a dynamical system that

is an important (but debated) facet of the physics of galaxies. Magnetic fields play a pivotal role because they control the density and distribution of cosmic rays, and they act on the dynamics if the gas. Much of the physics involved in this interplay is encoded in the structure of interstellar magnetic fields. Observations of synchrotron emission and its polarization, as

---

★ Corresponding author: A. Bracco,
e-mail: andrea.bracco@cea.fr

well as Faraday rotation and dust polarization, provide the means to characterize the structure of magnetic fields within galaxies (Haverkorn 2015; Lazarian & Pogosyan 2016; Beck 2016).

Since dust grains are mixed with interstellar gas, dust polarization data are well suited to investigate the physical coupling between the gas dynamics and the magnetic field structure, in other words to characterize magnetohydrodynamical (MHD) turbulence in the interstellar medium (ISM; Brandenburg & Lazarian 2013; Falceta-Gonçalves et al. 2014). Anisotropic dust grains tend to align with their longer axes perpendicular to the local magnetic field, and thus their emission is polarized perpendicular to the magnetic field projection on the plane of the sky (POS). The polarization fraction, p, the ratio between the polarized and total intensities of dust thermal emission, depends on the dust polarization properties and the grain alignment efficiency, but also on the structure of the magnetic field (Lazarian 2007). Thus, information on the magnetic field structure is encoded in the Stokes Q and U maps, as well as in the polarization angle ψ and fraction p.

For a long time, observations of dust polarization from the diffuse ISM were limited to stellar polarization data available for a discrete set of lines of sight (LOS; Heiles 2000). The *Planck*[1] data opened a new perspective on this topic. For the first time, we have maps of the dust polarization in emission over the full sky (Planck Collaboration I 2016). The *Planck* maps greatly supersede, in sensitivity and statistical power, the data available from earlier ground-based and balloon-borne observations (e.g. Benoît et al. 2004; Ponthieu et al. 2005; Ward-Thompson et al. 2009; Koch et al. 2010; Poidevin et al. 2014; Matthews et al. 2014).

Several studies have already used the *Planck* data to investigate the link between the dust polarization maps and the structure of the Galactic magnetic field (GMF). Planck Collaboration Int. XIX (2015) presented the first analysis of the polarized sky as seen at 353 GHz (the most sensitive *Planck* channel for polarized thermal dust emission), focusing on the statistics of p and ψ. The comparison with synthetic polarized emission maps, computed from simulations of anisotropic MHD turbulence, shows that the turbulent structure of the GMF is able to reproduce the main statistical properties of p and ψ in nearby molecular clouds (Planck Collaboration Int. XX 2015). This comparison shows that the mean orientation of the GMF with respect to the LOS plays a major role in the quantitative analysis of these statistical properties. An important result is that in the diffuse ISM, the filamentary structure of matter is observed to be statistically aligned with the GMF (McClure-Griffiths et al. 2006; Clark et al. 2014; Planck Collaboration Int. XXXII 2016; Kalberla et al. 2016).

The spatial structure of the polarization angle has been characterized in Planck Collaboration Int. XIX (2015) using the angle dispersion function $\mathcal{S}$ (see Eq. (1) in Hildebrand et al. 2009; and Eq. (6) in Planck Collaboration Int. XIX 2015). The map of $\mathcal{S}$ highlights long, narrow structures of high $\mathcal{S}$ that trace abrupt changes of ψ at the interfaces between extended areas within which the polarization angle is ordered. Falgarone et al. (2015) found a correlation between the structures in $\mathcal{S}$ and large velocity shears in incompressible magnetized turbulence. The structures seen in the *Planck* data bear a morphological resemblance

to features associated with Faraday rotation in gradient maps of polarized synchrotron emission at 1.4 and 2.3 GHz (Gaensler et al. 2011; Iacobelli et al. 2014), which have been related to fluctuations in the GMF and in the ionized gas density in MHD turbulence (Burkhart et al. 2012). Filamentary structures in rotation measure synthesis maps from LOFAR (the Low-Frequency Array) data (Jelić et al. 2015) have been shown to be correlated with the GMF orientation inferred from the *Planck* dust polarization (Zaroubi et al. 2015). At microwave frequencies, the dust polarization has been demonstrated to be correlated with synchrotron polarization, free from Faraday rotation (Planck Collaboration Int. XXII 2015; Choi & Page 2015). Both emission processes trace the same GMF, but the correlation is not one-to-one due to the difference in the distribution of dust and relativistic electrons in the Galaxy. Jaffe et al. (2013) and Planck Collaboration Int. XLII (2016) described the difficulties faced when trying to reproduce the *Planck* dust polarization data with existing models of the large-scale GMF (Jaffe et al. 2010; Sun & Reich 2010; Jansson & Farrar 2012), which are mainly constrained by synchrotron emission and Faraday rotation measures of extragalactic radio sources.

The GMF structure is also relevant for the modelling of polarized Galactic foregrounds in analyses of the CMB. Thermal emission from Galactic dust is the main polarized foreground at frequencies above 100 GHz (Planck Collaboration X 2016). Planck Collaboration Int. XXX (2016) presented the polarized dust angular power spectra C_ℓ^{EE} and C_ℓ^{BB}, providing cosmologists with a characterization of the dust foreground to CMB polarization. Planck Collaboration Int. XXXVIII (2016) showed that the correlation between the filamentary structure of matter and the GMF orientation may account for the E and B asymmetry, as well as the TE correlation, reported in the analysis of the power spectra of the *Planck* 353 GHz polarization maps.

Within this broad context, the motivations and objectives of this paper are twofold. First, we extend the analysis of the *Planck* dust polarization maps to the high Galactic latitudes in the southern sky. This part of the sky is of specific relevance to on-going and future CMB polarization observations performed from Antarctica and Chile (e.g. Errard et al. 2016). It was masked in the Planck Collaboration Int. XIX (2015) analysis because of residual systematic errors in the data. The polarization maps at 353 GHz (Planck Collaboration I 2016; Planck Collaboration VIII 2016) that have been made publicly available by the *Planck* consortium[2] are now suitable for such an analysis. Second, we introduce a modelling framework that relates the dust polarization to the GMF structure, its mean orientation, and a statistical description of its random (turbulent) component. This framework is also a step towards a modelling tool for the dust polarization, which may be used to assess component-separation methods in the analysis of CMB polarization (e.g. Planck Collaboration IX 2016; Planck Collaboration X 2016).

Our data analysis procedure focuses on the southern Galactic cap, the cleanest part of the sky that is directly relevant to CMB observations, in particular those carried out with ground-based telescopes from Antarctica and Chile[3]. This is also the part of the sky where the LOS through the Galaxy is the shortest, and hence is the region best suited to characterize the turbulent component of the GMF.

The paper is organized as follows. We present the *Planck* data in Sect. 2. Section 3 introduces our model of the
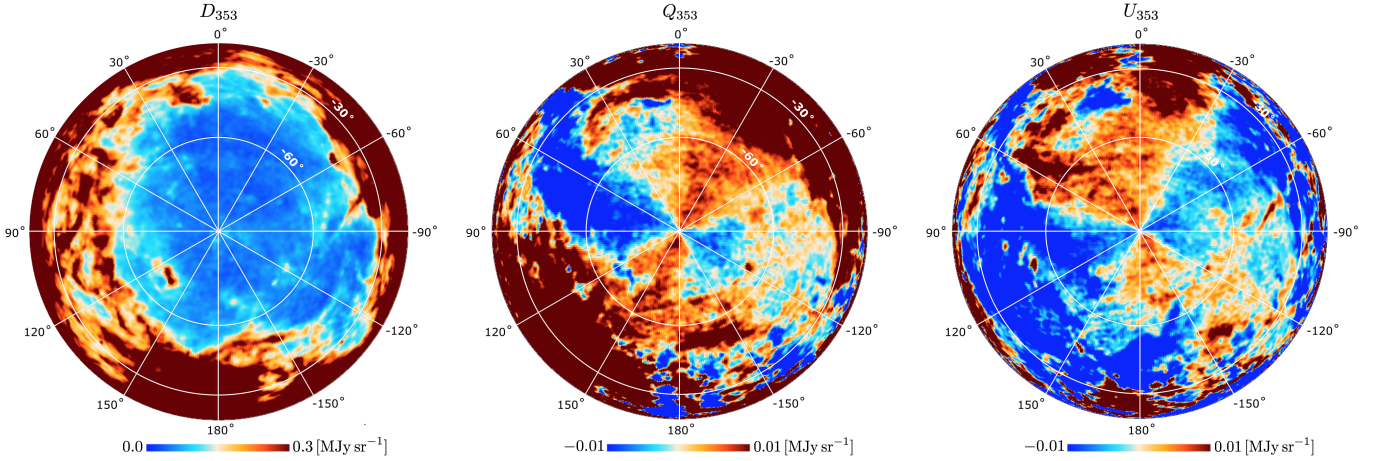
Fig. 1. Orthographic projections centred on the south Galactic pole of the *Planck* dust emission intensity, D_{353} (*left*), and the Stokes Q_{353} (*centre*) and U_{353} (*right*) maps, at 353 GHz. A grid of Galactic coordinates is included, labelled in degrees. East is on the left of the maps and the west on the right. We note that the U_{353} map is in the `HEALPix` (or CMB) polarization convention, which corresponds to $-U_{353}$ in the IAU convention.

GMF structure in the solar neighbourhood and in Sect. 4 we estimate the mean orientation of the GMF in the solar neighbourhood. In Sect. 5, we characterize the turbulent component of the GMF. The data analysis is based on a phenomenological model that we discuss in Sect. 6, which also contains our future perspectives. The paper's results are summarized in Sect. 7. The approximations made to compute the Stokes parameters are presented in Appendix A.

2. Data and conventions

We first introduce the data that we will use, discussing the conventions assumed in the analysis of polarization, and presenting the polarization parameters determined around the south Galactic pole.

2.1. Description of the data

The *Planck* satellite observed the polarized sky in seven frequency bands from 30 to 353 GHz (Planck Collaboration I 2014). In this paper, we only use the data from the High Frequency Instrument (HFI, Lamarre et al. 2010) at the highest frequency, 353 GHz, where the dust emission is the brightest.

We use the publicly available 353 GHz Stokes Q and U (hereafter, Q_{353} and U_{353}) maps (central and right panels in Fig. 1) and the associated noise maps made with the five independent consecutive sky surveys of the *Planck* cryogenic mission. We refer to publications by the Planck Collaboration for details of the processing of HFI data, including mapmaking, photometric calibration, and photometric uncertainties (Planck Collaboration I 2016; Planck Collaboration VII 2016; Planck Collaboration VIII 2016). The Q_{353} and U_{353} maps are corrected for spectral leakage as described in Planck Collaboration VIII (2016). For the dust total intensity at 353 GHz we use the model map, D_{353}, derived from a modified blackbody fit to the *Planck* data at $\nu \geq 353$ GHz, and IRAS at $\lambda = 100\,\mu$m (Planck Collaboration XI 2014, left panel in Fig. 1). The data used in this fit are corrected for zodiacal emission and CMB anisotropies. D_{353} has a also a lower noise than the corresponding 353 GHz Stokes I *Planck* map. The Q_{353} and U_{353} maps are initially constructed with an effective beamsize of $4'8$, and D_{353} at $5'$. The

three maps are in `HEALPix` format[4] with a pixelization $N_{\rm side} = 2048$. To increase the signal-to-noise ratio at high Galactic latitudes below $-60°$, we smooth the three maps to 1° resolution using a Gaussian approximation to the *Planck* beam. We reduce the `HEALPix` resolution to $N_{\rm side} = 128$ ($30'1$ pixels) after smoothing. For the polarization maps, we apply the `ismoothing` routine of `HEALPix`, which decomposes the Q and U maps into E and B maps, applies Gaussian smoothing in harmonic space, and transforms the smoothed E and B back into Q and U maps at $N_{\rm side} = 128$ resolution.

2.2. Applied conventions in polarization

In terms of Q_{353}, U_{353}, and D_{353}, the quantities p and ψ, are defined as

$$p = \frac{\sqrt{Q_{353}^2 + U_{353}^2}}{D_{353}},$$
$$\psi = \frac{1}{2}\tan^{-1}(-U_{353}, Q_{353}), \tag{1}$$

where the minus sign in ψ is needed to change the `HEALPix`-format maps (or "COSMO convention" for the FITS keyword `POLCONV`) into the International Astronomical Union (IAU) convention for ψ, measured from the local direction to the north Galactic pole with increasing positive values towards the east. Moreover, in this paper we use the version of the inverse tangent function with two signed arguments to resolve the π ambiguity (ψ corresponds to orientations not to directions).

When considering dust polarization, the Stokes parameters for linear polarization are integral quantities of the optical depth (see Appendix A and Planck Collaboration Int. XX 2015). An empirical expression for p is

$$p = p_0 F \cos^2 \gamma, \tag{2}$$

where γ is the angle between the mean orientation of the GMF and the POS. Therefore, the projection factor, $\cos^2 \gamma$, carries information on the orientation of the GMF with respect to the POS. In particular, dust polarization vanishes where the GMF points directly towards or away from the observer. Hereafter,

---

[4] Górski et al. (2005), `http://healpix.sf.net`
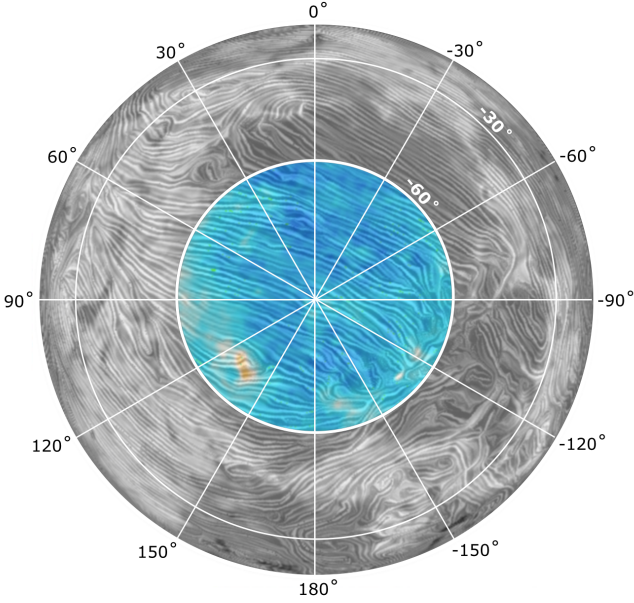
Fig. 2. *Planck* D_{353} (same as in the left panel of Fig. 1) with the "drapery" pattern, orthogonal to the polarization orientation, produced with the LIC algorithm. The part of the sky at $b < -60°$ has been highlighted in colour in this figure.

$p_0 = p_{dust} R$ is the effective dust polarization fraction, which combines the intrinsic polarization fraction of dust grains p_{dust} (the ratio between the polarization and average cross-sections of dust, as defined in Planck Collaboration Int. XX 2015) and R, the Rayleigh reduction factor (related to the degree of dust grain alignment with the GMF; Greenberg 1968; Lee & Draine 1985). The factor R is equal to 1 for perfect grain alignment. The factor F accounts for the depolarization due to variations of the GMF orientation along the LOS and within the beam.

2.3. Polarization parameters of the southern Galactic cap

Planck Collaboration Int. XIX (2015) characterized the polarized sky at 353 GHz at low and intermediate Galactic latitudes. Now, with the maps released in early 2015 (Planck Collaboration I 2016), we can extend this analysis to the high Galactic latitudes of the southern sky. In this work, we focus on the region around the south Galactic pole (Galactic latitude $b < -60°$), which is well suited to study emission from dust in the diffuse ISM, and directly relevant to study the dust foreground for CMB polarization.

We compute p and ψ from the Stokes parameters in Fig. 1 at a resolution of $1°$. Because of the square of Q and U, and the contribution from noise, p cannot be computed directly from Eq. (1) at high Galactic latitudes where the *Planck* signal-to-noise is low. A number of algorithms have been proposed (e.g. Montier et al. 2015) to derive unbiased estimates of p; here, we use the p_{MAS} estimator presented in Plaszczynski et al. (2014).

Figure 2 shows a map of the Planck dust emission intensity, D_{353}, with the drapery pattern of ψ, rotated by $\pi/2$, produced with the linear integral convolution (LIC) algorithm (Cabral & Leedom 1993) as in Planck Collaboration Int. XXXV (2016) and Planck Collaboration I (2016). This map reveals a high degree of order in ψ at $b < -60°$ (blue region). Figure 3 shows the normalized distributions of the polarization fraction from the p_{MAS} unbiased estimator, over the whole sky (in black) and at $b < -60°$ (in green). We also show the uncertainty on p_{MAS} at high latitude (green-shaded area) due to the error on the zero level of
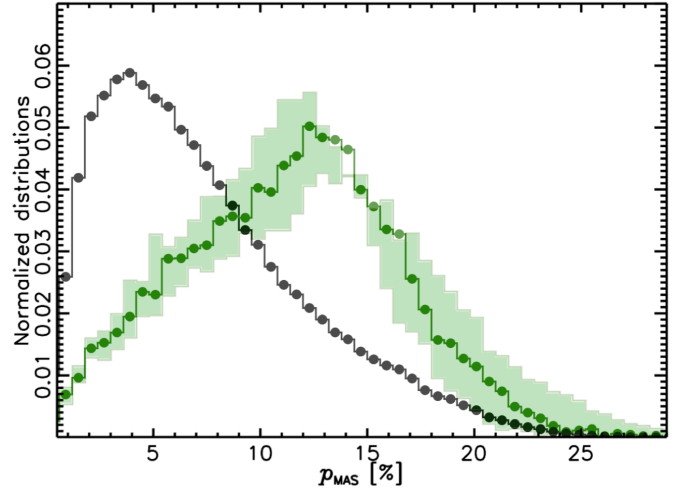
Fig. 3. Normalized distributions of the polarization fraction from the p_{MAS} debiased estimator (see text). The black distribution shows p_{MAS} over the whole sky. The green distribution shows p_{MAS} at $b < -60°$. The green-shaded area represents the 1σ error on p_{MAS} at high latitude.

D_{353} as estimated by Planck Collaboration XI (2014). Both distributions indicate a wide range of p_{MAS} values up to 25%. The main difference at low p_{MAS} values is likely caused by depolarization from LOS variations of the GMF orientation closer to the Galactic plane (Planck Collaboration Int. XIX 2015).

How do we explain the high p_{MAS} values and the observed dispersion in the distribution? As we will show, the GMF structure in the solar neighbourhood is essential to consider when answering this question.

3. Model framework

The polarization of thermal dust emission results from the alignment of elongated grains with respect to the GMF (Stein 1966; Hildebrand 1988). Within the hypothesis that grain polarization properties, including alignment, are homogeneous, the structure of the dust polarization sky reflects the structure of the GMF combined with that of matter. Throughout the paper, we assume that this hypothesis applies to the diffuse ISM, where radiative torques provide a mechanism to efficiently align grains (Dolginov & Mitrofanov 1976; Hoang & Lazarian 2014; Andersson et al. 2015). Our data modelling focuses on the structure of the GMF. This section describes the model framework (Sect. 3.1) and how we proceed to fit it to the data (Sect. 3.2).

3.1. Magnetic field modelling

We now introduce the framework we use to model the GMF structure within the solar neighbourhood. The integral equations of the Stokes I, Q and U parameters are recalled in Appendix A.

We follow earlier works (e.g. Chandrasekhar & Fermi 1953; Hildebrand et al. 2009), expressing the GMF ($\boldsymbol{B}$) as the sum of its mean ($\boldsymbol{B}_0$) and turbulent ($\boldsymbol{B}_t$) components:

$$\boldsymbol{B} = \boldsymbol{B}_0 + \boldsymbol{B}_t. \tag{3}$$

We introduce and discuss the assumptions we make about each of these two components.

Our model aims at describing dust polarization towards the southern Galactic cap at Galactic latitudes $b \leq -60°$. We focus

on the solar neighbourhood and thereby ignore the structure of the GMF on Galaxy-wide scales. We also ignore the change of its orientation from the disk to the halo (Haverkorn 2015) because dust emission arises mainly from a thin disk. The dust scale height is not measured in the solar neighbourhood, but modelling of the dust emission from the Milky Way indicates that the dust scale height at the solar distance to the Galactic centre is approximately 200 pc (Drimmel & Spergel 2001). Observations of the edge-on spiral galaxy NGC 891, a galaxy analogous to the Milky Way, give a comparable scale height of around 150 pc (Bocchio et al. 2016). These estimates are in agreement with the scale height of the neutral atomic gas in the Milky Way, inferred from H I observations (Dickey & Lockman 1990; Kalberla et al. 2007). Hence, we assume that the vector B_0 has a fixed orientation, which represents the mean orientation of the GMF in the solar neighbourhood.

Radio observations of synchrotron emission and polarization reveal a wealth of structures down to pc and sub-pc scales (e.g. Reich et al. 2004; Gaensler et al. 2011; Iacobelli et al. 2013, 2014), such as filaments, canals, lenses, and rings, which carry valuable information about B_t (Fletcher & Shukurov 2006). Heiles (1995) and Haverkorn (2015) reviewed observations that characterize this random component, concluding that it has a strength of about 5 μG, comparable to that of B_0. Jones et al. (1992) reached a similar conclusion from stellar polarization data.

The turbulent component of the GMF is significant. To take it into account, we follow earlier works (e.g. Waelkens et al. 2009; Fauvet et al. 2011), modelling each component of the B_t vector with Gaussian realizations. To model dust polarization over the celestial sphere, earlier studies (e.g. Miville-Deschênes et al. 2008; Fauvet et al. 2011; O'Dea et al. 2012) computed independent realizations of the components of B_t for each LOS. This approach ignores the angular coherence of B_t over the sky, which, however, is essential to match the correlated patterns seen in the *Planck* maps of the dust p and ψ (Planck Collaboration Int. XIX 2015). Because of this, we use a different method. We model B_t with Gaussian realizations on the celestial sphere, computed for an angular power spectrum C_ℓ scaling as a power-law ℓ^{α_M} for $\ell \geq 2$. The amplitude of the spectrum is parametrized by the ratio f_M between the standard deviation of $|B_t|$ and $|B_0|$.

Our spectrum does not have a low ℓ cut-off, which would represent the scale of energy injection of the turbulent energy cascade. Here since we compare the model and the data over a field with an angular extent of 60° (about 1 radian), we implicitly assume that the injection scale is larger than, or comparable to, the scale height of the dust emission (approximately 200 pc, Drimmel & Spergel 2001). The scale of the warm ionized medium (WIM) is larger (about 1–1.5 kpc, Gaensler et al. 2008), but the WIM is not a major component of the dust emission from the diffuse ISM (Planck Collaboration Int. XVII 2014). The range of distances involved in the modelling of dust polarization at high Galactic latitudes is small because there is little interstellar matter within the local bubble, i.e. within 50–100 pc of the Sun (Lallement et al. 2014). The local bubble may extend to larger distances towards the Galactic poles, but this possibility is not well constrained by existing data. In any case, it is reasonable to assume that most of the dust emission at high Galactic latitudes arises from a limited range of distances, which sets a rough correspondence between angles and physical scales in our model.

To compute the Stokes parameters, we approximate the integration along the line of sight (LOS) with a sum over a set of N polarization layers with independent realizations of B_t. The

layers are a phenomenological means to represent the variation of B_t along the LOS. Our modelling of B_t is continuous over the celestial sphere, while we use a set of independent orientations along the LOS. At first sight, this may be considered as physically inconsistent. However, in Sect. 6, we relate the polarization layers to the density structure and to the correlation length of B_t along the LOS. Our modelling does not take into account explicitly the density structure of matter along the LOS; the source function (presented in Eqs. (A.1b) and (A.1c)) is assumed to be constant along the LOS. It also ignores the alignment observed between the filamentary structure of the diffuse ISM and the magnetic field.

3.2. Data fitting in three steps: A, B, and C

Our model has six parameters: the two coordinates defining the orientation of B_0; f_M quantifying the dispersion of B around B_0; the number of layers, N; the index α_M; and the effective polarization fraction of dust emission, p_0. The parameters are not all fitted simultaneously because they are connected to the data in different ways. The coordinates of B_0 relate to the large-scale patterns in the Q_{353} and U_{353} maps and they do not depend on the other parameters. The triad of parameters f_M, N, and α_M describe statistical properties of the polarization maps. We determine f_M, N, and p_0 simultaneously by fitting the 1-point statistics of both ψ and p. To constrain α_M it is necessary to use 2-point statistics (i.e. power spectra); this is not done in this paper, but will be the specific topic of a future paper.

In the following two sections, we present three steps in our data-fitting, labelled steps A, B, and C. Step A only takes into account the mean field B_0. In Sect. 4, we determine the orientation of B_0 by fitting the regular patterns seen in the *Planck* Q_{353} and U_{353} maps shown in Fig. 1. The other two steps involve both B_0 and B_t, as required to reproduce the 1-point statistics of ψ and p. In step B (Sect. 5), B_t is computed from random realizations on the sphere. In this step, the depolarization due to changes in the orientation of B_t along the LOS is accounted for with an F factor in Eq. (2) that is uniform over the sky. This simplifying assumption is often made in analysing polarization data. Step C in Sect. 5.3 is an extension of step B, where we introduce variations of the F factor over the sky by summing Stokes parameters over N polarization layers along the LOS.

4. Mean orientation of the magnetic field

In this step A of our data modelling, we determine the orientation of the mean field B_0, ignoring B_t.

4.1. Description of step A

We show that the ordered magnetic field produces well-defined polarization patterns in the Q_{353} and U_{353} maps, resulting from the variation across the observed region of the angle between the LOS and the ordered field.

Given a Cartesian reference frame *xyz*, each point on the sphere can be identified by a pair of angular coordinates, hereafter the Galactic longitude and latitude, l and b. The reference frame is chosen to be centred at the observer with $\hat{z} = (0, 0, 1)$ pointing towards the north Galactic pole, $\hat{x} = (1, 0, 0)$ towards the Galactic centre, and $\hat{y} = (0, 1, 0)$ towards positive Galactic longitude.

We define the uniform direction of B_0 through the unit vector $\hat{B}_0$, which depends on the pair of coordinates (l_0, b_0) as
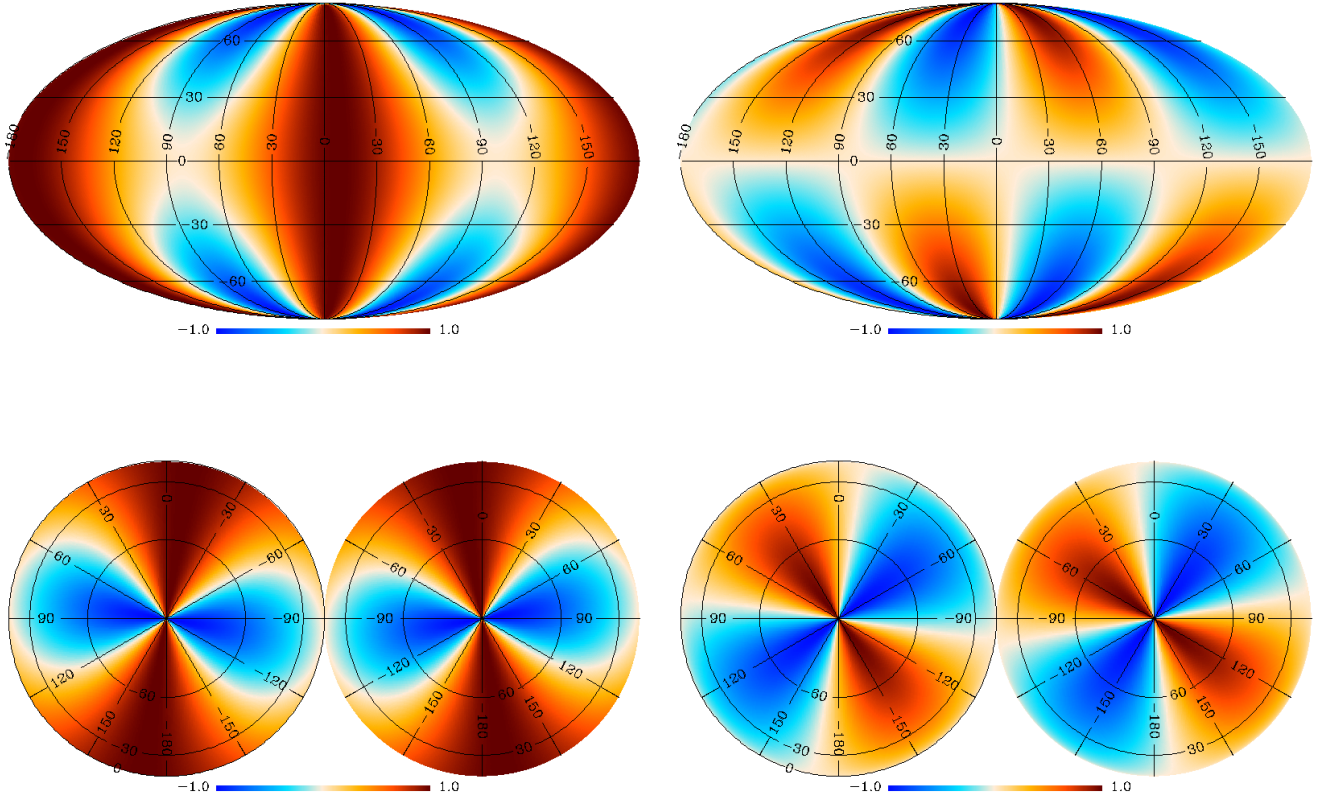
Fig. 4. Mollweide (*top*) and orthographic (*bottom*) projections of the model Stokes parameters, q_A (*left*) and u_A (*right*), for a uniform direction of the GMF towards $(l_0, b_0) = (80°, 0°)$; these are roughly the values inferred from starlight polarization (Heiles 1996). The orthographic projections are centred on the Galactic poles. Galactic coordinates in degrees are shown on all plots.

$\hat{\boldsymbol{B}}_0 = (\cos l_0 \cos b_0, \sin l_0 \cos b_0, \sin b_0)$. We define the generic LOS unit vector $\hat{\boldsymbol{r}}$ as $(\cos l \cos b, \sin l \cos b, \sin b)$ on a full-sky `HEALPix` grid.

Combining $\hat{\boldsymbol{r}}$ and $\hat{\boldsymbol{B}}_0$, we can derive the POS component of $\hat{\boldsymbol{B}}_0$, $\hat{\boldsymbol{B}}_{0\perp}$, as

$$\hat{\boldsymbol{B}}_{0\perp} = \hat{\boldsymbol{B}}_0 - \hat{\boldsymbol{B}}_{0\parallel} = \hat{\boldsymbol{B}}_0 - (\hat{\boldsymbol{B}}_0 \cdot \hat{\boldsymbol{r}})\hat{\boldsymbol{r}}, \tag{4}$$

where $\hat{\boldsymbol{B}}_{0\parallel}$ is the component of $\hat{\boldsymbol{B}}_0$ along $\hat{\boldsymbol{r}}$. In order to define the ψ and γ angles for a given $\hat{\boldsymbol{r}}$, we need to derive the north and east directions, tangential to the sphere, which correspond to

$$\hat{\boldsymbol{n}} = \frac{(\hat{\boldsymbol{r}} \times \hat{\boldsymbol{z}}) \times \hat{\boldsymbol{r}}}{|(\hat{\boldsymbol{r}} \times \hat{\boldsymbol{z}}) \times \hat{\boldsymbol{r}}|},$$
$$\hat{\boldsymbol{e}} = \frac{-\hat{\boldsymbol{r}} \times \hat{\boldsymbol{n}}}{|\hat{\boldsymbol{r}} \times \hat{\boldsymbol{n}}|}, \tag{5}$$

respectively. The polarization angle is perpendicular to that between $\hat{\boldsymbol{B}}_{0\perp}$ and $\hat{\boldsymbol{n}}$, and γ the angle between $\hat{\boldsymbol{B}}_0$ and $\hat{\boldsymbol{B}}_{0\perp}$. From Eqs. (4) and (5), we derive

$$\psi_A = \arccos\left(\frac{\hat{\boldsymbol{B}}_{0\perp} \cdot \hat{\boldsymbol{n}}}{|\hat{\boldsymbol{B}}_{0\perp}|}\right) + 90°,$$
$$\cos^2 \gamma_A = 1 - |\hat{\boldsymbol{B}}_0 \cdot \hat{\boldsymbol{r}}|^2, \tag{6}$$

where the subscript "A" stands for step A, and the sign of arccos is imposed by the sign of $\hat{\boldsymbol{B}}_{0\perp} \cdot \hat{\boldsymbol{e}}$.

Using Eqs. (1) and (2), we can produce an analytical expressions for the modelled Stokes parameters normalized to the total

intensity times $p_0 F$, q_A and u_A, as follows:

$$q_A = \cos^2 \gamma_A \cos 2\psi_A;$$
$$u_A = -\cos^2 \gamma_A \sin 2\psi_A. \tag{7}$$

We stress that q_A and u_A only show patterns generated by projection effects. For illustration, in Fig. 4 we present maps of q_A and u_A for a uniform direction of the GMF towards $(l_0, b_0) = (80°, 0°)$, roughly the direction inferred from starlight polarization data (Heiles 1996). We note that the total intensity of dust emission also depends on the GMF geometry (Planck Collaboration Int. XX 2015). However, as detailed in Appendix A, this is a small effect that does not alter our results.

4.2. Fitting step A to the Planck data

At first glance, the "butterfly" patterns in the Q_{353} and U_{353} maps around the south Galactic pole in Fig. 1 resemble those produced with step A in Fig. 4. In order to find the orientation of $\hat{\boldsymbol{B}}_0$ that best fits the data, we explore the space of Galactic coordinates for (l_0, b_0), spanning Galactic longitudes between 0° and 180°, and latitudes between −90° and 90°. From Eqs. (1), (2), and (7), we simultaneously fit step A to Q_{353} and U_{353} with the corresponding errors, as

$$Q_{353} = p_{0,A} q_A D_{353},$$
$$U_{353} = p_{0,A} u_A D_{353}, \tag{8}$$

where the factor $p_{0,A}$ represents an average of the product $p_0 F$ in Eq. (2) over the region where we perform the fit. For each (l_0, b_0) pair we perform a linear fit to determine $p_{0,A}$. The fit is carried
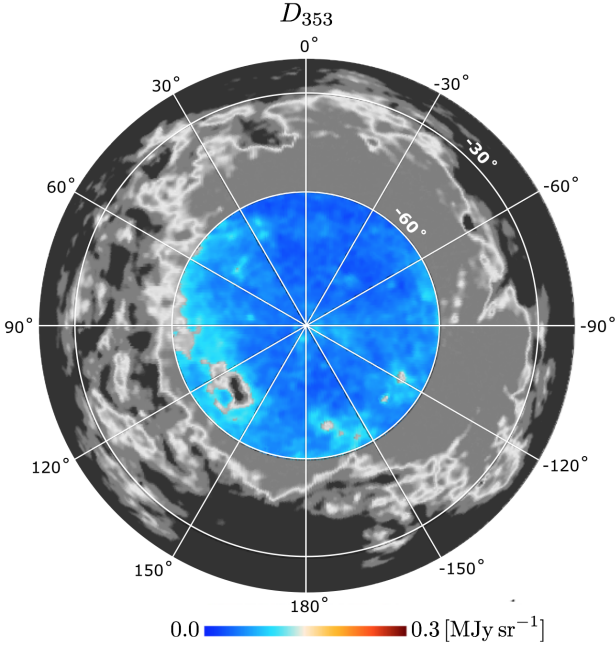
Fig. 5. Same as in the left panel of Fig. 1, but now highlighting the $b < -60°$ region, excluding the brightest clouds (in grey in the image), which has been used to fit the orientation of the mean magnetic field in step A of our model fit.

out for the southern polar cap at $b < -60°$, after masking the most intense localized structures around the south Galactic pole, as shown in Fig. 5. To remove these regions from the analysis, we fit a Gaussian profile to the histogram of pixel values of D_{353} below $b = -60°$. We then mask all pixels with $D_{353} > \bar{x}_D + 4\,\sigma_{\bar{x}_D}$, where $\bar{x}_D$ and $\sigma_{\bar{x}_D}$ are the mean and the standard deviation of the Gaussian fit.

The fit is done over an area of $2652\,\mathrm{deg}^2$, corresponding to 2652 independent data beams. Since the number of parameters is 3, the number of degrees of freedom, $N_{\mathrm{d.o.f.}}$, is large. We find a best-fit direction of the mean GMF towards Galactic coordinates $l_0 = 70° \pm 5°$ and $b_0 = 24° \pm 5°$. The value of $p_{0,\mathrm{A}}$ corresponding to this direction is $(12 \pm 1)\%$, which corresponds to the peak of the distribution of p_{MAS} in this area (see Fig. 3). The statistical errors are small but there are significant uncertainties on the three parameters from residual, uncorrected, systematic effects in the data. We quote these uncertainties, which we estimated repeating the fit on maps produced with ten different subsets of the data (Planck Collaboration 2015). We notice that, because of the 180° ambiguity in the definition of ψ, the opposite direction $(l_0 + \pi, -b_0)$ is an equivalent solution of our fit. However, the chosen solution is the closest to the mean GMF direction derived from observations of pulsars in the solar neighbourhood (Rand & Kulkarni 1989; Ferrière 2015), which, unlike dust polarization are sensitive to the sign of the GMF. Our determination of l_0 is in agreement with earlier values derived from starlight polarization (e.g. Heiles 1996). The positive value of b_0 is consistent with the positive sign of the median value of rotation measures derived from observations of extragalactic radio sources in the direction of the southern Galactic cap (Taylor et al. 2009; Mao et al. 2010). For illustration, we show the best-fit model maps of q_{A} and u_{A} around the south pole in Fig. 6.

We note that the obtained value of $p_{0,\mathrm{A}}$ is a substantial fraction of the maximum p (>18%) reported in Planck Collaboration Int. XIX (2015) at intermediate Galactic latitudes. We also stress that this value of $p_{0,\mathrm{A}}$ is only a lower limit to the effective dust

polarization fraction because step A does not take into account any depolarizing effects along the LOS, associated with variations of the GMF orientation.

5. Turbulent component of the magnetic field

The *Planck* maps show structures in polarization on a wide range of scales (Fig. 1), not accounted for by the single field orientation of step A, which we associate with the turbulent component of the magnetic field B_{t}. In Sects. 5.1 and 5.2, B_{t} is assumed to vary only across the sky (step B), while in Sect. 5.3, we take into account its variations both across the sky and along the LOS (step C).

5.1. Step B: dispersion of the polarization angle

In Sect. 4.2, we found that the best-fit orientation of B_0 in step A is given by $(l_0, b_0) = (70°, 24°)$. We can now obtain maps of the corresponding normalized Stokes parameters, $u_{0\mathrm{A}}$ and $q_{0\mathrm{A}}$, as well as a map of the associated polarization angle

$$\psi_{0\mathrm{A}} = \frac{1}{2}\tan^{-1}\left(-u_{0\mathrm{A}}, q_{0\mathrm{A}}\right). \tag{9}$$

The angle $\psi_{0\mathrm{A}}$ allows us to rotate, at each point on the sky, the reference direction used to compute the Stokes parameters (Q_{353}, U_{353}). With this new reference, the q_{A} map in Fig. 6 would be that of $\cos^2 \gamma_{\mathrm{A}}$, and u_{A} would be null (see Eq. (7)). To obtain the rotated values Q_{353}^R and U_{353}^R, we apply to the data the following rotation matrix (e.g. Delabrouille et al. 2009):

$$\begin{pmatrix} Q_{353}^{\mathrm{R}} \\ U_{353}^{\mathrm{R}} \end{pmatrix} = \begin{pmatrix} \cos 2\psi_{0\mathrm{A}} & \sin 2\psi_{0\mathrm{A}} \\ -\sin 2\psi_{0\mathrm{A}} & \cos 2\psi_{0\mathrm{A}} \end{pmatrix} \begin{pmatrix} Q_{353} \\ U_{353} \end{pmatrix}. \tag{10}$$

The maps of Q_{353}^R and U_{353}^R are shown in Fig. 7, where the butterfly patterns, caused by the uniform component of the GMF, are now removed by the change of reference. The polarization angle that can be derived from Q_{353}^R and U_{353}^R as

$$\psi_{\mathrm{R}} = \frac{1}{2}\tan^{-1}(-U_{353}^{\mathrm{R}}, Q_{353}^{\mathrm{R}}), \tag{11}$$

represents the dispersion of $B_\perp$ around $B_{0\perp}$. The histogram of ψ_{R} for $b < -60°$, shown in the top panel of Fig. 8 (black dots with Poisson noise as error bars), has a 1σ dispersion of $12°$.

To characterize B_{t}, it is necessary to account for projection effects (Falceta-Gonçalves et al. 2008; Planck Collaboration Int. XXXII 2016). Planck Collaboration Int. XXXII (2016) describes a geometric model, which we use in this paper to characterize the 3D dispersion of B with respect to B_0, given the histogram of ψ_{R}. Each component of B_{t} is obtained with an independent realization of a Gaussian field with an angular power spectrum equal to a power law of index α_{M}, for multipoles $\ell \geq 2$. The degree of alignment between B and B_0 is parameterized by f_{M}, which represents the ratio between the strengths of the turbulent and mean components of the GMF.

In the top panel of Fig. 8, we show that for $f_{\mathrm{M}} = 0.4$ the model reproduces the histogram of ψ_{R} fairly well. We computed 20 different Gaussian realizations to take into account the statistical variance of the model. The green line represents the average of the 20 realizations, whereas the green shaded regions are the $\pm 1\sigma$ (light) and $\pm 2\sigma$ (dark) variations of the model. In these calculations, as in Planck Collaboration Int. XXXII (2016), the spectral index α_{M} has a value of -1.5. This specific choice
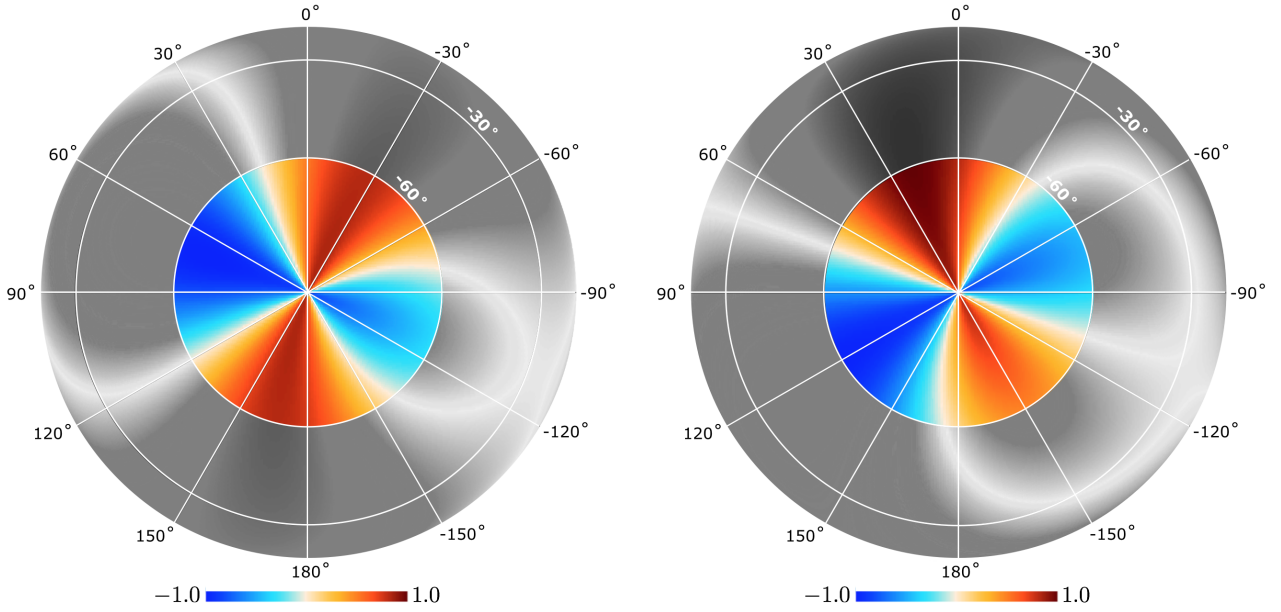
Fig. 6. Step A: orthographic projections of q_A (*left*) and u_A (*right*) centred on the south Galactic pole, for the best-fit direction of the uniform GMF towards $(l_0, b_0) = (70°, 24°)$. The sky at $b > -60°$ is masked here.
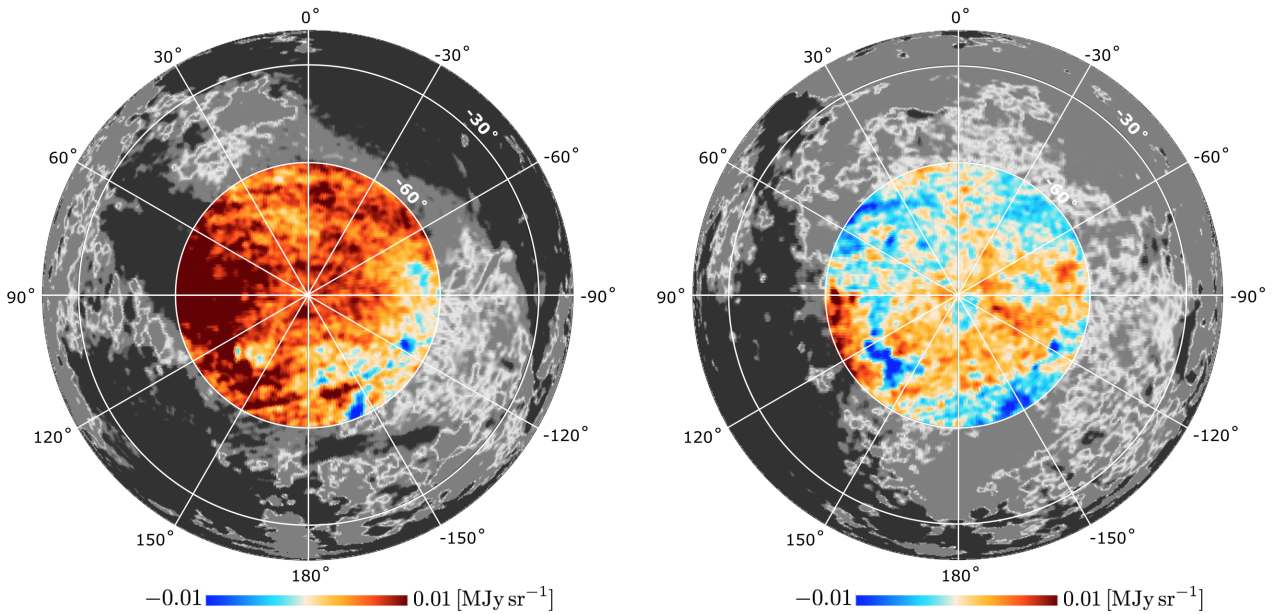
Fig. 7. Orthographic projections centred on the south Galactic pole of Q_{353}^R (*left*) and U_{353}^R (*right*), the Stokes parameters in a reference frame rotated with respect to the best-fit direction of the uniform component of the GMF towards $(l_0, b_0) = (70°, 24°)$. The sky for the masked $b > -60°$ region appears in grey.

does not impact the distribution of ψ_R, or that of p. However, we note that the variance of the histogram, i.e. the dispersion of histogram values between independent realizations, increases for decreasing values of α_M.

5.2. Step B: histogram of the polarization fraction

We showed that the structure of the GMF on the sphere allows us to reproduce ψ_R over the southern Galactic cap. Here, we characterize the distribution of p at $b < -60°$ and we show that step B is not sufficient to describe the data.

As already discussed above, the noise bias on p represents an intrinsic problem. To circumvent it, we compute unbiased values of p^2 by multiplying Stokes parameters from subsets of the data. Doing this, instead of using p_{MAS} as in Sect. 2.3, gives us control over the level of noise in the data, as we now demonstrate. We use the year-maps (denoted by the indices "Y1" and "Y2"), which have uncorrelated instrumental noise, and compute p^2 as

$$p^2 = \frac{Q_{353}^{Y1} Q_{353}^{Y2} + U_{353}^{Y1} U_{353}^{Y2}}{(D_{353})^2}. \tag{12}$$

We also estimate p^2 from the DetSet maps (made from different subsets of detectors, see Planck Collaboration 2015), and we find
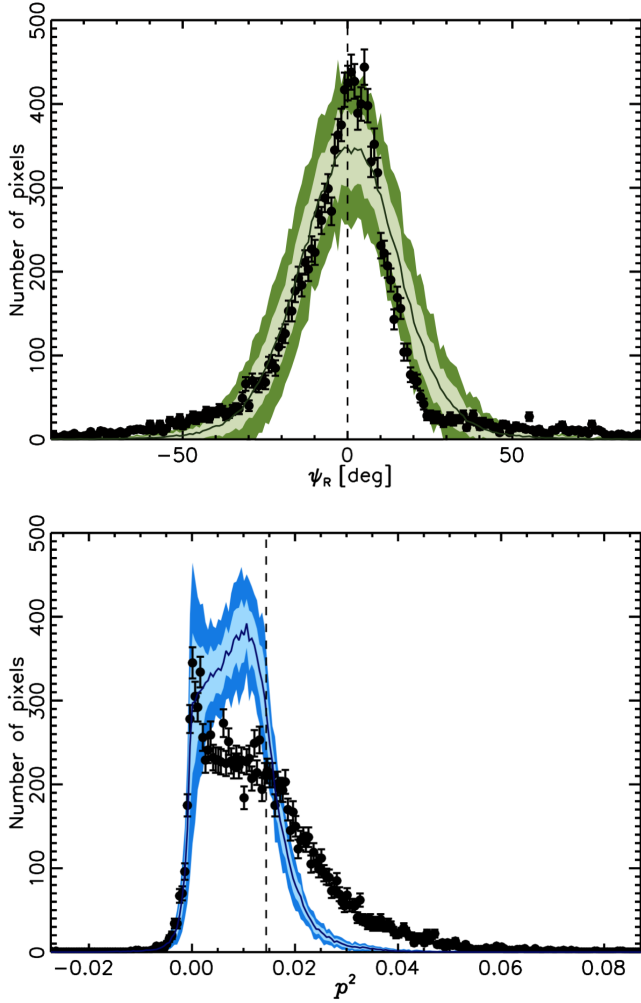
**Fig. 8.** Results of step B. *Top*: histogram of ψ_R, the polarization angle inferred from the Stokes parameters rotated with respect to the best-fit uniform direction of the GMF (Q_{353}^R and U_{353}^R), over the southern Galactic cap (black dots). The error bars represent the Poisson noise within each bin of the histogram. The green line represents the mean of the step B results for $f_M = 0.4$ over 20 different realizations. The green shaded regions correspond to $\pm 1\sigma$ (light green) and $\pm 2\sigma$ (dark green) variations of the model. *Bottom*: histogram of p^2 obtained when combining the Year 1 and Year 2 maps (black dots). The error bars here represent the Poisson noise within each bin of the histogram. Step B is now shown in blue. The dashed vertical line corresponds to a value of the polarization fraction of 12%.

good agreement between the two estimates using distinct subsets of the data.

In order to model p^2, we make use of the results obtained from fitting steps A and B to the data. Given $\boldsymbol{B}_0$, pointing towards $(l_0, b_0) = (70°, 24°)$, we add $\boldsymbol{B}_t$ to it with normalization parameter $f_M = 0.4$. In doing so, we now produce the two variables q_B and u_B, as q_A and u_A in Eq. (7), where now the angles take into account the turbulent component of the GMF. We then make realizations of the *Planck* statistical noise (n_{Qi} and n_{Ui}, with $i = 1, 2$), and, as in Eq. (8), we produce two pairs of independent samples of modelled Stokes Q and U as

$$Q_{Mi} = p_0 q_B D_{353} + n_{Qi},$$
$$U_{Mi} = p_0 u_B D_{353} + n_{Ui}, \qquad (13)$$
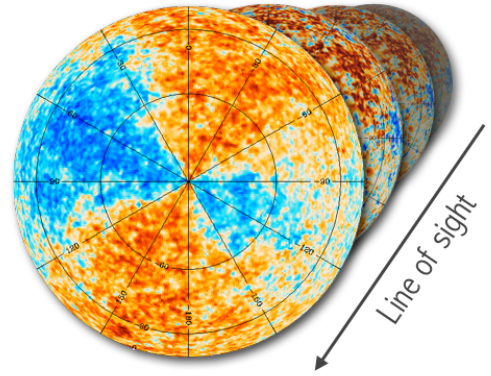
Fig. 9. Cartoon illustrating, for step C, the integration of q_C along the LOS, with four distinct polarization layers for the same value of f_M and the same mean orientation of the GMF. Each map in this cartoon is a realization of the model.

in which $i = 1, 2$ and $p_0 = 12\%$. Thus, the modelled p^2 results from

$$p_M^2 = \frac{Q_{M1} Q_{M2} + U_{M1} U_{M2}}{(D_{353})^2}. \qquad (14)$$

In the bottom panel of Fig. 8, we show the comparison between the histograms of p^2 for the data (black dots) and for the model. In particular, we present the average over 20 realizations of step B (blue line) and the corresponding $\pm 1\sigma$ (light blue shaded region) and $\pm 2\sigma$ (dark blue) variations. The dashed vertical line refers to the value of $p_0 = 12\%$. We notice that our modelling of p^2 seems to appropriately take into account the data noise since it nicely fits the negative p^2 values, which result from noise in the combination of the individual year maps.

However, from Fig. 8 it is clear that our description of the GMF structure using step B does not provide a satisfactory characterization of the distribution of p^2. The data show a more prominent peak in the distribution towards very low p^2 values than seen in the model, for which the histogram peaks near the value of p_0. Moreover, the large dispersion in the data, also found by Planck Collaboration Int. XIX (2015) at intermediate Galactic latitudes, produces a long tail in the distribution towards high values of p^2, which is not reproduced by the model.

5.3. Step C: line-of-sight depolarization

Now we consider the effect of depolarization, associated with variations of the GMF orientation along the LOS. This additional step is essential to account for the dispersion of p and correctly estimate the amplitude of the turbulent component of the GMF with respect to its mean component because the dispersion of the polarization angle is reduced by averaging along the LOS (Myers & Goodman 1991; Jones et al. 1992; Houde et al. 2009).

Figure 9 illustrates step C with a simple cartoon. In order to account for the LOS integration that characterizes the polarization data, we produce N distinct maps of $q_{B,i}$ and $u_{B,i}$ (with i from 1 to N), for a common, but freely varying value of f_M, while fixing $\alpha_M = -1.5$ (as in step B), and for the best-fit orientation of $\boldsymbol{B}_0$ obtained with step A. The Gaussian realizations of $\boldsymbol{B}_t$ are different for each layer. All layers have the same $\boldsymbol{B}_0$ but an independent $\boldsymbol{B}_t$ in Eq. (3). Then, we model the LOS depolarization by averaging the Stokes parameters over the N layers
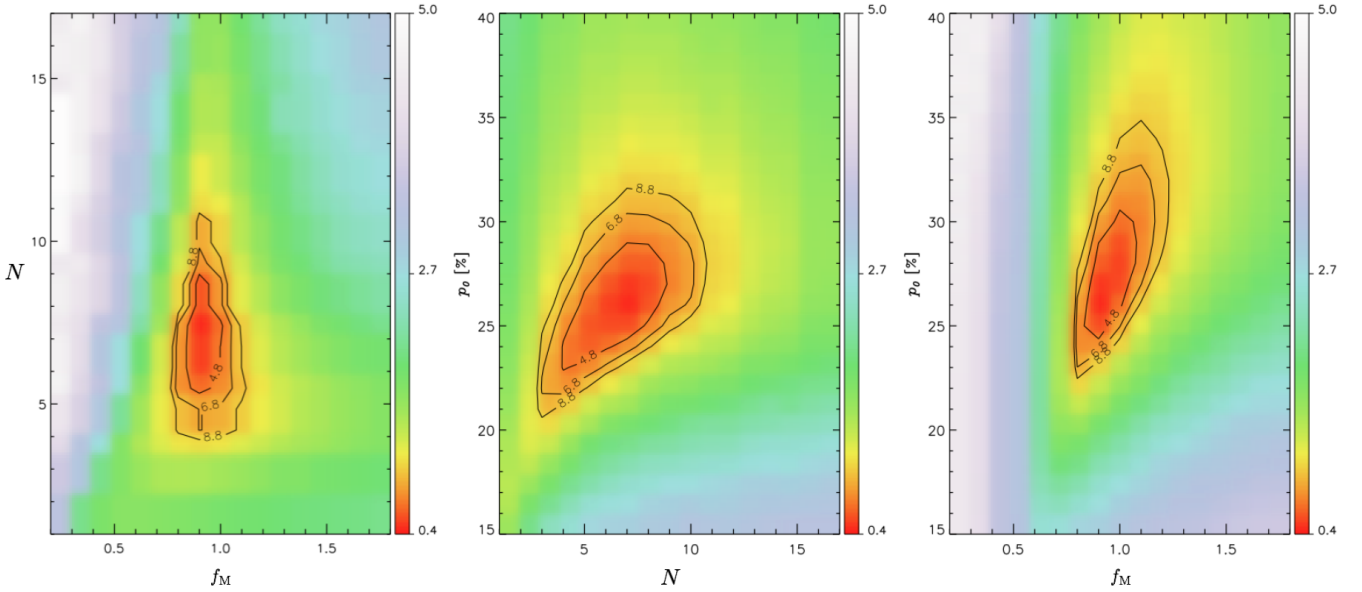
Fig. 10. Results of step C. Maps of $\chi^2_{\rm tot}$ from the fit of step C to the data for $p_0 = 26\%$ (*left*), for $N = 7$ (*centre*), and for $f_{\rm M} = 0.9$ (*right*). The three maps show in colours and with contours the quantity $\log_{10}(\chi^2_{\rm tot})$.

as follows:

$$q_{\rm C} = \frac{\sum_{i=1}^{N} q_{{\rm B},i}}{N};$$

$$u_{\rm C} = \frac{\sum_{i=1}^{N} u_{{\rm B},i}}{N}. \qquad (15)$$

We follow the same procedure as in Sects. 5.1 and 5.2, with $q_{\rm B}$ and $u_{\rm B}$ replaced by $q_{\rm C}$ and $u_{\rm C}$, to obtain model distributions of p^2 and $\psi_{\rm R}$.

Given $\alpha_{\rm M}$, the modelled distributions of p^2 and $\psi_{\rm R}$ depend on three main parameters, namely p_0, $f_{\rm M}$, and N. We fit the data exploring the parameter spaces of p_0 between 15% and 40% with steps of 1%, of $f_{\rm M}$ between 0.2 and 1.8 with steps of 0.1, and of N between 1 and 17 with steps of 1. The distributions of p^2 and $\psi_{\rm R}$ have about 200 bins each. For each triad of parameters we compute maps of the reduced χ^2 for the combined p^2 and $\psi_{\rm R}$ fit, using

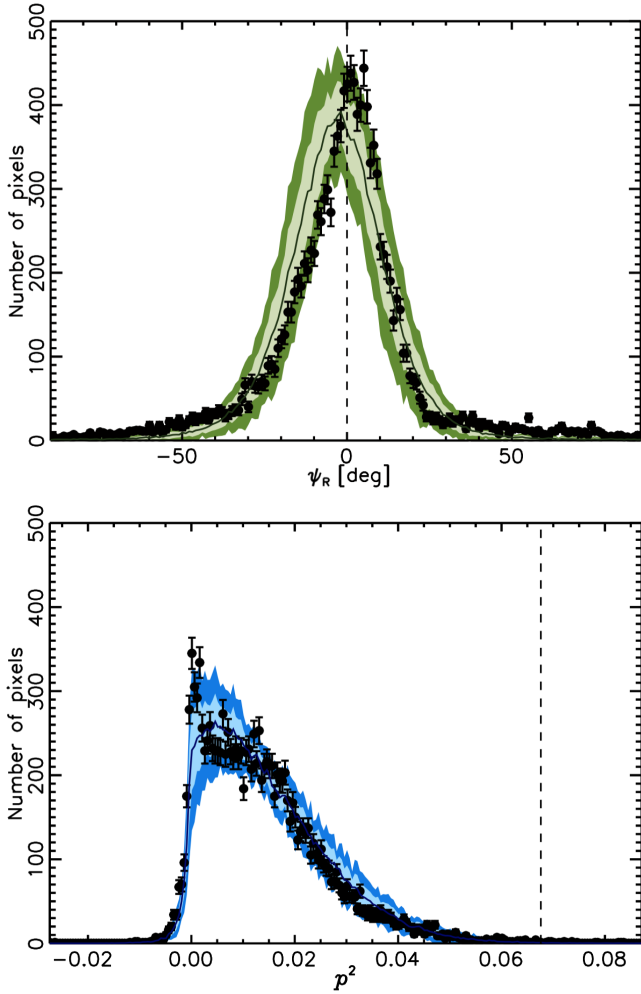$$\chi^2_{\rm tot} = \chi^2_{p^2} + \chi^2_{\psi_{\rm R}}, \qquad (16)$$

where in computing the χ^2 distributions we fit the data with the mean of the 20 realizations, and we add their dispersion in quadrature to the error bar of the observations. Fitting the distribution of $\psi_{\rm R}$ between $-40°$ and $40°$ (where most of the data lie), we obtain a best fit for a minimum $\chi^2_{\rm tot}$ of 2.8, for $p_0 = 26\%$, $f_{\rm M} = 0.9$, and $N = 7$. In Fig. 10 we show three maps of $\chi^2_{\rm tot}$; each one corresponds to the parameter space for two parameters given the best-fit value of the third one. The $\chi^2_{\rm tot}$ maps reveal some correlation among the three parameters. The variance of each model among the 20 different realizations represents the dominant uncertainty of the fit, and it is correlated between the bins of the histogram. Repeating the χ^2-minimization for each one of the 20 realizations, the fit constrains the range of values for the main parameters to $0.8 < f_{\rm M} < 1$, $5 < N < 9$, and $23\% < p_0 < 29\%$. Step C generates a mean value of the depolarization factor F that is about 0.5, and thus leads to an estimate of p_0 twice larger than in step A. The best-fit value of $(26 \pm 3)\%$ is comparable with the maximum value of the observed reported in Planck Collaboration Int. XIX (2015).

As in Fig. 8, the histograms of p^2 and $\psi_{\rm R}$ for the best-fit triad are shown in the bottom and top panels of Fig. 11, respectively. The top panel of Fig. 11 shows that if we consider a few ($N \simeq 7$) independent polarization layers along the LOS, this provides us with an estimate of $f_{\rm M}$ that is closer to equality between the turbulent and mean components of the GMF than for step B (for which $N = 1$, see Sect. 5.1). A value of $f_{\rm M} = 0.9$ with $N = 1$ would generate a much broader distribution of $\psi_{\rm R}$ than the observed one. The bottom panel of Fig. 11 shows that step C, unlike step B, can reproduce the histogram of p^2 quite well. The combination of a small number of independent polarization layers along the LOS produces the large dispersion in p^2 that is observed in the data.

Our results show that, in order to reproduce the p^2 distribution seen in the data, only a small number of polarization layers is needed. In Fig. 12, we present the effect of changing N on the distribution of p^2 obtained with step C as $p^2_{\rm C} = q^2_{\rm C} + u^2_{\rm C}$. In this case noise is not added and we fix $l_0 = 70°$, $b_0 = 24°$, and $f_{\rm M} = 0.9$, but vary N from 1 (dark blue line) to 100 (dark red line). The figure shows that for an increasing number of layers because of the central-limit theorem, the model distributions tend to rapidly converge towards a low p^2 value, without the broad dispersion observed in the data. For large values of N, the width of the p^2 distribution is dominated by the projection factor, $\cos^2 \gamma$, in Eq. (7). Note that the histogram of $p^2_{\rm C}$ for $N = 1$ is not directly comparable with the modelled p^2 distribution in Fig. 8 because it does not include noise.

6. Discussion

We have presented a phenomenological model that is able to describe the 1-point statistics of p and ψ for the *Planck* dust polarization data around the south Galactic pole, using a few parameters to describe the uniform and turbulent components of the GMF. We stress that our model is not entirely physical and certainly not unique. We made several assumptions, including: a single orientation of the mean field $\boldsymbol{B}_0$; a uniform ratio $f_{\rm M}$ of the turbulent to mean strengths of the GMF along the LOS; a

Fig. 12. Model histograms of p_C^2 obtained around the south Galactic pole from step C, using $f_M = 0.9$, and with the value of N varying from 1 (dark blue) to 100 (dark red).

spectrum analysis of the dust emission from the Polaris cloud in Miville-Deschênes et al. (2010). The superposition of such clouds fits with our model, where the angular correlation is described with a continuous power spectrum, different from our ansatz for the radial correlation.

As shown for the diffuse ISM (Clark et al. 2014; Planck Collaboration Int. XXXII 2016; Planck Collaboration Int. XXXVIII 2016; Kalberla et al. 2016), the GMF orientation is correlated with the structure of matter as traced by H I or dust emission. Our modelling does not include the density structure of the ISM, nor does it include the correlation between matter and the magnetic field orientation; however, the polarization layers could phenomenologically represent distinct matter structures along the LOS. In this interpretation the GMF orientations are not completely uncorrelated. Although each CNM structure has a different turbulent component of the GMF, they share the same mean component. This correlation between the values of ψ of individual structures and those measured for the background emission in their surroundings is in fact observed in the *Planck* data (Planck Collaboration Int. XXXII 2016).

Observations of H I in absorption and emission have shown that, in the solar neighbourhood, about 60% of all H I arises from the warm neutral medium (WNM) and gas that is out of thermal equilibrium (Heiles & Troland 2003). Moreover, the diffuse ISM also includes the WIM, which accounts for about 25% of the gas column density (Reynolds 1989). These diffuse and warm components of the ISM are expected to contribute to the dust emission observed at high Galactic latitudes, both in intensity and in polarization. This contribution, which may be dominant, cannot be described by a small number of localized structures. For such media, the layers acquire a physical meaning if their spacing corresponds approximately to the correlation length of the turbulent component of the GMF.

6.2. Correlation length of the magnetic field

In their modelling of dust polarization in molecular clouds, Myers & Goodman (1991) and Planck Collaboration Int. XXXV (2016) introduced a correlation length that is associated with the coupling scale through collisions between ions and neutrals. For the *Planck* data relating to the diffuse ISM, we propose a different interpretation. Following Eilek (1989), we derive the correlation length of the turbulent component of the GMF (l_c)
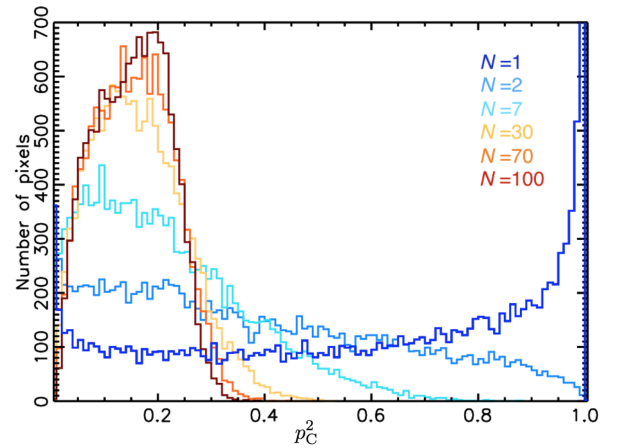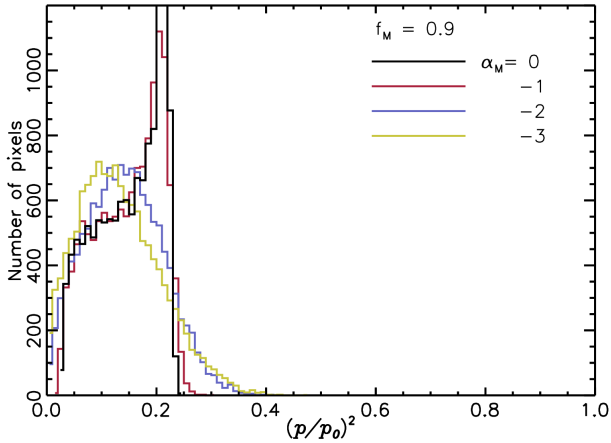

Fig. 11. Results of step C. This is the same as in Fig. 8, but with the model histograms now corresponding to step C with $f_M = 0.9$, $N = 7$, and $p_0 = 26\%$ (dashed-vertical line).

fixed value for the number of polarization layers, N, independent of the total dust intensity (unlike what was considered by Jones et al. 1992); and isotropy of the turbulent component, $\boldsymbol{B}_t$. These assumptions restrict us from fitting the data over a larger portion of the sky than the southern Galactic cap. For the time being, we limit our study to this sky area. We now discuss the interpretation of our model in relation to the ISM physics and we present future perspectives on the modelling.

6.1. Density structure of the ISM

Our description of the turbulent component of the GMF along the LOS is based on a finite number of independent layers, rather than on a continuous variation computed from the power spectrum of the GMF, as was included in some earlier models (e.g. Miville-Deschênes et al. 2008; O'Dea et al. 2012; Planck Collaboration Int. XLII 2016). The density structure of the diffuse ISM provides one argument in favour of this approximation.

If we are in practice observing a finite number of localized density structures from the cold neutral medium (CNM) along the LOS, then the discretization of the GMF orientation is appropriate. Such structures appear as extended features on the sky in dust emission maps, with a power-law power spectrum. This statement is exemplified by the images and the power

Fig. 13. Model histograms of p^2 normalized to unity with p_0, obtained for a continuously varying GMF orientation along the LOS, with $f_M = 0.9$ for several values of α, between 0 (black curve) and -3 (yellow curve). To facilitate the comparison of the histogram of $(p/p_0)^2$ with that in Fig. 12, we have used the same bin width (0.01) to compute both histograms.

from the 2-point auto-correlation function, C_B, of each of the three components of B_t:

$$\int C_B(s)\,ds = l_c\,\sigma_B^2, \tag{17}$$

where s is the lag of C_B along one given direction and σ_B is the dispersion of B_i. In this framework, the number of correlation lengths along the LOS is $N_c = L/l_c$, where L is the effective extent of matter along the LOS. We compute C_B from Gaussian realizations of B_i for power-law spectra[5], and, from there, N_c integrating Eq. (17) up to the lag where $C_B = 0$. N_c depends on the spectral index α of the power spectrum of the components of B_t. We find values of N_c of 16, 10, 6, and 5 for spectral indices of the power law spectrum $\alpha = -1.5, -2, -2.5$, and -3, respectively.

We can now compute the Stokes parameters for this continuous description of B_t and the mean orientation, B_0 (determined in Sect. 4), through the integral equations described in Appendix A, for several values of α using a constant source function as in step C. The Gaussian realizations and the integrals are computed over 1024 of points along each LOS at $b < -60°$. In this approach, used earlier by Miville-Deschênes et al. (2008), O'Dea et al. (2012), there is no correlation of B_t between nearby pixels on the sky. Hence, we cannot produce realistic images but we do sample the 1-point distribution of p^2.

The histograms of p^2 (normalized to unity with p_0) are presented in Fig. 13 for several values of α, with $f_M = 0.9$ and no data noise. We use the same binning as in Fig. 12 to allow for a direct comparison between the two sets of histograms. The continuous description of B_t matches the standard deviation of ψ_R measured in the *Planck* data for $\alpha \simeq -3$. However, the corresponding histogram of $(p/p_0)^2$ in Fig. 13 is narrower than the one for $N = 7$ in Fig. 12, which fits the data better. We conclude that the number of polarization layers may be interpreted as the number of effective modes contributing to the variations of the orientation of B_t along the LOS within the WNM and WIM. From this view point, the low value of N derived from the data fit reflects the steepness of the power spectrum of B_t; however, this interpretation does not fully account for the data because it ignores the density structure of the diffuse ISM (i.e. the CNM).

---

[5] To a good approximation, $\sigma_B^2 - C_B$ can be fitted with a power law of the lag s.

6.3. Future perspectives

We now briefly outline a few future directions that could be taken to extend our data analysis and modelling.

We have started to investigate the impact of the GMF structure on the statistics of the polarization parameters. In an upcoming paper we will use the model presented in this work to reproduce the dust polarization power spectra measured by *Planck* (Planck Collaboration Int. XXX 2016) and constrain the value of α_M, the value of which is left open in this paper. Another future project will be to introduce the density structure and its correlation with the orientation of the GMF within each polarization layer. Such a study will enable us to assess the respective contributions of the density and the GMF structure to the statistics of the dust polarization data.

In the present work, we have aimed at providing a phenomenological method to relate the dust polarization at high Galactic latitudes to the structure of the GMF. We want to stress the simplicity of our approach, which allowed us to fit the large-scale patterns of the polarization sky and the one point statistics of ψ and p, measured towards the southern Galactic cap, with a few parameters. In a future paper we will extend the present study to a larger fraction of the high-latitude sky on both hemispheres to assess the ability of our model to describe the *Planck* 353 GHz dust polarization data over a larger area than the one considered in this study.

Our work is a main step towards a model which may be used to compute realizations of the dust polarization sky that fit the E, B and TE power spectra of dust polarization spectra reported in Planck Collaboration Int. XXX (2016) for the multipoles range $30 < \ell < 300$. Such simulated maps will be useful to assess the accuracy of component-separation methods in present and future CMB experiments designed to search the B mode CMB polarization expected from primordial gravity waves (BICEP2/Keck Array and Planck Collaborations 2015).

Planck Collaboration Int. XXXVIII (2016) and Clark et al. (2015) associated the asymmetry between EE and BB power spectra of dust polarization (i.e. $C_\ell^{BB} \simeq 0.5\,C_\ell^{EE}$, Planck Collaboration Int. XXX 2016) with the correlation between the structure of the GMF and the distribution of interstellar matter. Future models will need to take this correlation into account in order to realistically assess the accuracy to which, for a given experiment, dust and CMB polarization can be separated.

7. Summary

We have analysed the *Planck* maps of the Stokes parameters at high Galactic latitudes over the sky area $b < -60°$, which is well suited for describing the Galactic magnetic field (GMF) structure in the diffuse interstellar medium (ISM), and is directly relevant for cosmic microwave background (CMB) studies. We characterized the structure of the Stokes parameter maps at 353 GHz, as well as the statistics of the polarization fraction p and angle ψ. We presented simple geometrical models, which relate the data to the structure of the GMF in the solar neighbourhood. Combining models of the turbulent and ordered components of the GMF, we have reproduced the patterns of the Stokes Q and U maps at large angular scales, as well as the histograms of p and ψ. The main results of the paper are listed below.

– We find that the histogram of p of the southern Galactic cap has a similar dispersion as that measured over the whole sky, although with a smaller depolarization, caused by line-of-sight (LOS) variations of the GMF orientation, on and near the Galactic plane.

– The Stokes Q and U maps show regular patterns at large scales, which we associate with the mean orientation of the GMF in the solar neighbourhood. We build a geometric model and find a mean orientation towards Galactic coordinates $(l_0, b_0) = (70°, 24°)$, compatible with previous estimates. The fit also provides us with the average value of p at $b \leq -60°$, which is $(12 \pm 1)\%$.

– By means of a simple description of the turbulent component of the GMF (Gaussian and isotropic), we manage to account for both the dispersion of ψ and the histogram of p. The effect of depolarization caused by the GMF fluctuations along the LOS is introduced through an approximation where the integrals along the LOS are replaced by a discrete sum over only a few independent polarization layers. This approach successfully reproduces the p and ψ distributions using $N \simeq 4$–9 layers.

– The integration along the LOS generates a mean depolarization factor that is about 0.5 and thus leads to an estimate of p_0 about two times greater than the average value of p. The best-fit value of the effective polarization of dust, which combines the intrinsic polarization of dust grains and their degree of alignment with the GMF, is $(26 \pm 3)\%$.

– Our description of the turbulent component of the GMF corresponds to a rough equality between the turbulent and mean strengths of the GMF. The same conclusion was reached from modelling the dispersion of polarization angles measured for CNM filamentary structures by Planck Collaboration Int. XXXII (2016). We extend this to the diffuse ISM observed in the high latitude sky, which comprises both WNM and CNM gas.

The present study represents the first step towards the characterization of the magnetized properties of the diffuse ISM by means of the *Planck* data. We argue that both the density structure and the effective correlation length of the GMF contribute to the large dispersion of p observed in the data. This can be further investigated using MHD numerical simulations. The next step in our modelling of dust polarization at high Galactic latitudes will be to fit the E and B power spectra. This will constrain the spectral index of the GMF power spectrum, providing information on the turbulent energy cascade in the diffuse ISM. It is also a required step before using our model to compute simulated maps for assessing component-separation methods in CMB polarization projects.

References

Andersson, B.-G., Lazarian, A., & Vaillancourt, J. E. 2015, ARA&A, 53, 501

Beck, R. 2016, A&ARv, 24, 4

Benoît, A., Ade, P., Amblard, A., et al. 2004, A&A, 424, 571

BICEP2/Keck Array and Planck Collaborations 2015, Phys. Rev. Lett., 114, 101301

Bocchio, M., Bianchi, S., Hunt, L. K., & Schneider, R. 2016, A&A, 586, A8

Brandenburg, A., & Lazarian, A. 2013, Space Sci. Rev., 178, 163

Burkhart, B., Lazarian, A., & Gaensler, B. M. 2012, ApJ, 749, 145

Cabral, B., & Leedom, L. C. 1993, in Special Interest Group on GRAPHics and Interactive Techniques Proceedings, 263

Chandrasekhar, S., & Fermi, E. 1953, ApJ, 118, 113

Choi, S. K., & Page, L. A. 2015, J. Cosmology Astropart. Phys., 12, 020

Clark, S. E., Peek, J. E. G., & Putman, M. E. 2014, ApJ, 789, 82

Clark, S. E., Hill, J. C., Peek, J. E. G., Putman, M. E., & Babler, B. L. 2015, Phys. Rev. Lett., 115, 241302

Delabrouille, J., Cardoso, J., Le Jeune, M., et al. 2009, A&A, 493, 835

Dickey, J. M., & Lockman, F. J. 1990, ARA&A, 28, 215

Dolginov, A. Z., & Mitrofanov, I. G. 1976, Ap&SS, 43, 291

Drimmel, R., & Spergel, D. N. 2001, ApJ, 556, 181

Eilek, J. A. 1989, AJ, 98, 256

Errard, J., Feeney, S. M., Peiris, H. V., & Jaffe, A. H. 2016, J. Cosmology Astropart. Phys., 3, 052

Falceta-Gonçalves, D., Lazarian, A., & Kowal, G. 2008, ApJ, 679, 537

Falceta-Gonçalves, D., Kowal, G., Falgarone, E., & Chian, A. C.-L. 2014, Nonlin. Processes Geophys., 21, 587

Falgarone, E., Momferratos, G., & Lesaffre, P. 2015, in Magnetic Fields in Diffuse Media, eds. A. Lazarian, E. M. de Gouveia Dal Pino, & C. Melioli, Astrophys. Space Sci. Libr., 407, 227

Fauvet, L., Macías-Pérez, J. F., Aumont, J., et al. 2011, A&A, 526, A145

Ferrière, K. 2015, J. Phys. Conf. Ser., 577, 012008

Fletcher, A., & Shukurov, A. 2006, MNRAS, 371, L21

Gaensler, B. M., Madsen, G. J., Chatterjee, S., & Mao, S. A. 2008, PASA, 25, 184

Gaensler, B. M., Haverkorn, M., Burkhart, B., et al. 2011, Nature, 478, 214

Górski, K. M., Hivon, E., Banday, A. J., et al. 2005, ApJ, 622, 759

Greenberg, J. M. 1968, in Nebulae and Interstellar Matter, eds. B. M. Middlehurst, & L. H. Aller (The University of Chicago Press), 221

Haverkorn, M. 2015, in Magnetic Fields in Diffuse Media, eds. A. Lazarian, E. M. de Gouveia Dal Pino, & C. Melioli, Astrophys. Space Sci. Libr., 407, 483

Heiles, C. 1995, in The Physics of the Interstellar Medium and Intergalactic Medium, eds. A. Ferrara, C. F. McKee, C. Heiles, & P. R. Shapiro, ASP Conf. Ser., 80, 507

Heiles, C. 1996, ApJ, 462, 316

Heiles, C. 2000, AJ, 119, 923

Heiles, C., & Troland, T. H. 2003, ApJ, 586, 1067

Hildebrand, R. H. 1988, QJRAS, 29, 327

Hildebrand, R. H., Kirby, L., Dotson, J. L., Houde, M., & Vaillancourt, J. E. 2009, ApJ, 696, 567

Hoang, T., & Lazarian, A. 2014, MNRAS, 438, 680

Houde, M., Vaillancourt, J. E., Hildebrand, R. H., Chitsazzadeh, S., & Kirby, L. 2009, ApJ, 706, 1504

Iacobelli, M., Haverkorn, M., Orrú, E., et al. 2013, A&A, 558, A72

Iacobelli, M., Burkhart, B., Haverkorn, M., et al. 2014, A&A, 566, A5

Jaffe, T. R., Leahy, J. P., Banday, A. J., et al. 2010, MNRAS, 401, 1013

Jaffe, T. R., Ferrière, K. M., Banday, A. J., et al. 2013, MNRAS, 431, 683

Jansson, R., & Farrar, G. R. 2012, ApJ, 757, 14

Jelić, V., de Bruyn, A. G., Pandey, V. N., et al. 2015, A&A, 583, A137

Jones, T. J., Klebe, D., & Dickey, J. M. 1992, ApJ, 389, 602

Kalberla, P. M. W., Dedes, L., Kerp, J., & Haud, U. 2007, A&A, 469, 511

Kalberla, P. M. W., Kerp, J., Haud, U., et al. 2016, ApJ, 821, 117

Koch, P. M., Tang, Y.-W., & Ho, P. T. P. 2010, ApJ, 721, 815

Lallement, R., Vergely, J.-L., Valette, B., et al. 2014, A&A, 561, A91

Lamarre, J.-M., Puget, J.-L., Ade, P. A. R., et al. 2010, A&A, 520, A9

Lazarian, A. 2007, J. Quant. Spectr. Rad. Transf., 106, 225

Lazarian, A., & Pogosyan, D. 2016, ApJ, 818, 178

Lee, H. M., & Draine, B. T. 1985, ApJ, 290, 211

Mao, S. A., Gaensler, B. M., Haverkorn, M., et al. 2010, ApJ, 714, 1170

Matthews, T. G., Ade, P. A. R., Angilè, F. E., et al. 2014, ApJ, 784, 116

McClure-Griffiths, N. M., Dickey, J. M., Gaensler, B. M., Green, A. J., & Haverkorn, M. 2006, ApJ, 652, 1339

Miville-Deschênes, M.-A., Ysard, N., Lavabre, A., et al. 2008, A&A, 490, 1093

Miville-Deschênes, M.-A., Martin, P. G., Abergel, A., et al. 2010, A&A, 518, L104

Montier, L., Plaszczynski, S., Levrier, F., et al. 2015, A&A, 574, A136

Myers, P. C., & Goodman, A. A. 1991, ApJ, 373, 509

O'Dea, D. T., Clark, C. N., Contaldi, C. R., & MacTavish, C. J. 2012, MNRAS, 419, 1795

Planck Collaboration 2015, The Explanatory Supplement to the *Planck* 2015 results, http://wiki.cosmos.esa.int/planckpla/index.php/Main_Page (ESA)

Planck Collaboration I. 2014, A&A, 571, A1

Planck Collaboration XI. 2014, A&A, 571, A11

Planck Collaboration I. 2016, A&A, 594, A1
Planck Collaboration VII. 2016, A&A, 594, A7
Planck Collaboration VIII. 2016, A&A, 594, A8
Planck Collaboration IX. 2016, A&A, 594, A9
Planck Collaboration X. 2016, A&A, 594, A10
Planck Collaboration Int. XVII. 2014, A&A, 566, A55
Planck Collaboration Int. XIX. 2015, A&A, 576, A104
Planck Collaboration Int. XX. 2015, A&A, 576, A105
Planck Collaboration Int. XXII. 2015, A&A, 576, A107
Planck Collaboration Int. XXX. 2016, A&A, 586, A133
Planck Collaboration Int. XXXII. 2016, A&A, 586, A135
Planck Collaboration Int. XXXV. 2016, A&A, 586, A138
Planck Collaboration Int. XXXVIII. 2016, A&A, 586, A141
Planck Collaboration Int. XLII. 2016, A&A, 596, A103
Plaszczynski, S., Montier, L., Levrier, F., & Tristram, M. 2014, MNRAS, 439, 4048
Poidevin, F., Ade, P. A. R., Angile, F. E., et al. 2014, ApJ, 791, 43
Ponthieu, N., Macías-Pérez, J. F., Tristram, M., et al. 2005, A&A, 444, 327
Rand, R. J., & Kulkarni, S. R. 1989, ApJ, 343, 760
Reich, W., Fürst, E., Reich, P., et al. 2004, in The Magnetized Interstellar Medium, eds. B. Uyaniker, W. Reich, & R. Wielebinski, 45
Reynolds, R. J. 1989, ApJ, 339, L29
Stein, W. 1966, ApJ, 144, 318
Sun, X.-H., & Reich, W. 2010, Res. Astron. Astrophys., 10, 1287
Taylor, A. R., Stil, J. M., & Sunstrum, C. 2009, ApJ, 702, 1230
Waelkens, A., Jaffe, T., Reinecke, M., Kitaura, F. S., & Enßlin, T. A. 2009, A&A, 495, 697
Ward-Thompson, D., Sen, A. K., Kirk, J. M., & Nutter, D. 2009, MNRAS, 398, 394
Zaroubi, S., Jelić, V., de Bruyn, A. G., et al. 2015, MNRAS, 454, L46

[1] APC, AstroParticule et Cosmologie, Université Paris Diderot, CNRS/IN2P3, CEA/lrfu, Observatoire de Paris, Sorbonne Paris Cité, 10 rue Alice Domon et Léonie Duquet, 75205 Paris Cedex 13, France

[2] Aalto University Metsähovi Radio Observatory and Dept of Radio Science and Engineering, PO Box 13000, 00076 Aalto, Finland

[3] African Institute for Mathematical Sciences, 6-8 Melrose Road, Muizenberg 7945, Cape Town, South Africa

[4] Agenzia Spaziale Italiana Science Data Center, via del Politecnico snc, 00133 Roma, Italy

[5] Aix-Marseille Université, CNRS, LAM (Laboratoire d'Astrophysique de Marseille) UMR 7326, 13388 Marseille, France

[6] Astrophysics Group, Cavendish Laboratory, University of Cambridge, J J Thomson Avenue, Cambridge CB3 0HE, UK

[7] Astrophysics & Cosmology Research Unit, School of Mathematics, Statistics & Computer Science, University of KwaZulu-Natal, Westville Campus, Private Bag X54001, 4000 Durban, South Africa

[8] CITA, University of Toronto, 60 St. George St., Toronto, ON M5S 3H8, Canada

[9] CNRS, IRAP, 9 Av. colonel Roche, BP 44346, 31028 Toulouse Cedex 4, France

[10] California Institute of Technology, Pasadena, CA 91125, USA

[11] Computational Cosmology Center, Lawrence Berkeley National Laboratory, Berkeley, CA 94720, USA

[12] Consejo Superior de Investigaciones Científicas (CSIC), 28006 Madrid, Spain

[13] DTU Space, National Space Institute, Technical University of Denmark, Elektrovej 327, 2800 Kgs. Lyngby, Denmark

[14] Département de Physique Théorique, Université de Genève, 24 quai E. Ansermet, 1211 Genève 4, Switzerland

[15] Departamento de Astrofísica, Universidad de La Laguna (ULL), 38206 La Laguna, Tenerife, Spain

[16] Departamento de Física, Universidad de Oviedo, Avda. Calvo Sotelo s/n, 33007 Oviedo, Spain

[17] Department of Astrophysics/IMAPP, Radboud University Nijmegen, PO Box 9010, 6500 GL Nijmegen, The Netherlands

[18] Department of Physics & Astronomy, University of British Columbia, 6224 Agricultural Road, Vancouver, British Columbia, Canada

[19] Department of Physics and Astronomy, Dana and David Dornsife College of Letter, Arts and Sciences, University of Southern California, Los Angeles, CA 90089, USA

[20] Department of Physics and Astronomy, University College London, London WC1E 6BT, UK

[21] Department of Physics, Gustaf Hällströmin katu 2a, University of Helsinki, 00014 Helsinki, Finland

[22] Department of Physics, Princeton University, Princeton, NJ 08544, USA

[23] Department of Physics, University of California, Santa Barbara, CA 93106, USA

[24] Department of Physics, University of Illinois at Urbana-Champaign, 1110 West Green Street, Urbana, Illinois, USA

[25] Dipartimento di Fisica e Astronomia G. Galilei, Università degli Studi di Padova, via Marzolo 8, 35131 Padova, Italy

[26] Dipartimento di Fisica e Astronomia, Alma Mater Studiorum, Università degli Studi di Bologna, Viale Berti Pichat 6/2, 40127 Bologna, Italy

[27] Dipartimento di Fisica e Scienze della Terra, Università di Ferrara, via Saragat 1, 44122 Ferrara, Italy

[28] Dipartimento di Fisica, Università La Sapienza, P.le A. Moro 2, 00185 Roma, Italy

[29] Dipartimento di Fisica, Università degli Studi di Milano, via Celoria 16, 20133 Milano, Italy

[30] Dipartimento di Fisica, Università degli Studi di Trieste, via A. Valerio 2, 34127 Trieste, Italy

[31] Dipartimento di Matematica, Università di Roma Tor Vergata, via della Ricerca Scientifica 1, 00133 Roma, Italy

[32] Discovery Center, Niels Bohr Institute, Copenhagen University, Blegdamsvej 17, 2100 Copenhagen, Denmark

[33] European Space Agency, ESAC, Planck Science Office, Camino bajo del Castillo, s/n, Urbanización Villafranca del Castillo, 28692 Villanueva de la Cañada, Madrid, Spain

[34] European Space Agency, ESTEC, Keplerlaan 1, 2201 AZ Noordwijk, The Netherlands

[35] Gran Sasso Science Institute, INFN, viale F. Crispi 7, 67100 L'Aquila, Italy

[36] HGSFP and University of Heidelberg, Theoretical Physics Department, Philosophenweg 16, 69120 Heidelberg, Germany

[37] Haverford College Astronomy Department, 370 Lancaster Avenue, Haverford, Pennsylvania, USA

[38] Helsinki Institute of Physics, Gustaf Hällströmin katu 2, University of Helsinki, 00014 Helsinki, Finland

[39] INAF–Osservatorio Astronomico di Padova, Vicolo dell'Osservatorio 5, 35122 Padova, Italy

[40] INAF–Osservatorio Astronomico di Roma, via di Frascati 33, 00040 Monte Porzio Catone, Italy

[41] INAF–Osservatorio Astronomico di Trieste, via G.B. Tiepolo 11, 40127 Trieste, Italy

[42] INAF/IASF Bologna, via Gobetti 101, 40129 Bologna, Italy

[43] INAF/IASF Milano, via E. Bassini 15, 20133 Milano, Italy

[44] INFN – CNAF, viale Berti Pichat 6/2, 40127 Bologna, Italy

[45] INFN, Sezione di Bologna, viale Berti Pichat 6/2, 40127 Bologna, Italy

[46] INFN, Sezione di Ferrara, via Saragat 1, 44122 Ferrara, Italy

[47] INFN, Sezione di Roma 1, Università di Roma Sapienza, P.le Aldo Moro 2, 00185 Roma, Italy

[48] INFN, Sezione di Roma 2, Università di Roma Tor Vergata, via della Ricerca Scientifica 1, 00185 Roma, Italy

[49] INFN/National Institute for Nuclear Physics, via Valerio 2, 34127 Trieste, Italy

[50] Imperial College London, Astrophysics group, Blackett Laboratory, Prince Consort Road, London, SW7 2AZ, UK

[51] Institut d'Astrophysique Spatiale, CNRS, Univ. Paris-Sud, Université Paris-Saclay, Bât. 121, 91405 Orsay Cedex, France

[52] Institut d'Astrophysique de Paris, CNRS (UMR 7095), 98bis boulevard Arago, 75014 Paris, France

[53] Institute of Astronomy, University of Cambridge, Madingley Road, Cambridge CB3 0HA, UK

[54] Institute of Theoretical Astrophysics, University of Oslo, Blindern, 0371 Oslo, Norway

[55] Instituto de Astrofísica de Canarias, C/Vía Láctea s/n, La Laguna, 38205 Tenerife, Spain

[56] Instituto de Física de Cantabria (CSIC-Universidad de Cantabria), Avda. de los Castros s/n, 39005 Santander, Spain

[57] Istituto Nazionale di Fisica Nucleare, Sezione di Padova, via Marzolo 8, 35131 Padova, Italy

[58] Jet Propulsion Laboratory, California Institute of Technology, 4800 Oak Grove Drive, Pasadena, CA 31109, USA

[59] Jodrell Bank Centre for Astrophysics, Alan Turing Building, School of Physics and Astronomy, The University of Manchester, Oxford Road, Manchester, M13 9PL, UK

[60] Kavli Institute for Cosmological Physics, University of Chicago, Chicago, IL 60637, USA

[61] Kavli Institute for Cosmology Cambridge, Madingley Road, Cambridge, CB3 0HA, UK

[62] LAL, Université Paris-Sud, CNRS/IN2P3, 91898 Orsay, France

[63] LERMA, CNRS, Observatoire de Paris, 61 avenue de l'Observatoire, 75014 Paris, France

[64] Laboratoire AIM, IRFU/Service d'Astrophysique – CEA/DSM – CNRS – Université Paris Diderot, Bât. 709, CEA-Saclay, 91191 Gif-sur-Yvette Cedex, France

[65] Laboratoire Traitement et Communication de l'Information, CNRS (UMR 5141) and Télécom ParisTech, 46 rue Barrault, 75634 Paris Cedex 13, France

[66] Laboratoire de Physique Subatomique et Cosmologie, Université Grenoble-Alpes, CNRS/IN2P3, 53 rue des Martyrs, 38026 Grenoble Cedex, France

[67] Laboratoire de Physique Théorique, Université Paris-Sud 11 & CNRS, Bâtiment 210, 91405 Orsay, France

[68] Lawrence Berkeley National Laboratory, Berkeley, California, USA

[69] Max-Planck-Institut für Astrophysik, Karl-Schwarzschild-Str. 1, 85741 Garching, Germany

[70] Mullard Space Science Laboratory, University College London, Surrey RH5 6NT, UK

[71] Nicolaus Copernicus Astronomical Center, Bartycka 18, 00-716 Warsaw, Poland

[72] Niels Bohr Institute, Copenhagen University, Blegdamsvej 17, 2100 Copenhagen, Denmark

[73] Nordita (Nordic Institute for Theoretical Physics), Roslagstullsbacken 23, 106 91 Stockholm, Sweden

[74] SISSA, Astrophysics Sector, via Bonomea 265, 34136 Trieste, Italy

[75] School of Physics and Astronomy, University of Nottingham, Nottingham NG7 2RD, UK

[76] Simon Fraser University, Department of Physics, 8888 University Drive, Burnaby BC, Canada

[77] Sorbonne Université-UPMC, UMR 7095, Institut d'Astrophysique de Paris, 98bis boulevard Arago, 75014 Paris, France

[78] Space Sciences Laboratory, University of California, Berkeley, CA 94720, USA

[79] Sub-Department of Astrophysics, University of Oxford, Keble Road, Oxford OX1 3RH, UK

[80] The Oskar Klein Centre for Cosmoparticle Physics, Department of Physics, Stockholm University, AlbaNova, 106 91 Stockholm, Sweden

[81] UPMC Univ. Paris 06, UMR 7095, 98bis boulevard Arago, 75014 Paris, France

[82] Université de Toulouse, UPS-OMP, IRAP, 31028 Toulouse Cedex 4, France

[83] University of Granada, Departamento de Física Teórica y del Cosmos, Facultad de Ciencias, 18071 Granada, Spain

[84] Warsaw University Observatory, Aleje Ujazdowskie 4, 00-478 Warszawa, Poland

Appendix A: Approximations for dust polarization

In this Appendix, we detail the approximations made to model the Stokes parameters for linear polarization from dust emission. For the sake of clarity, we recall the integral equations of the Stokes parameters I, Q, and U from Planck Collaboration Int. XX (2015):

$$I = \int S_\nu \, e^{-\tau_\nu} \left[1 - p_0 \left(\cos^2 \gamma - \frac{2}{3} \right) \right] d\tau_\nu; \tag{A.1a}$$

$$Q = \int p_0 \, S_\nu \, e^{-\tau_\nu} \cos(2\psi) \cos^2 \gamma \, d\tau_\nu; \tag{A.1b}$$

$$U = \int p_0 \, S_\nu \, e^{-\tau_\nu} \sin(2\psi) \cos^2 \gamma \, d\tau_\nu. \tag{A.1c}$$

Here τ_ν is the optical depth and S_ν is the source function of dust emission, while p_0 and the angles (ψ, γ) are the same as in Sect. 2.2.

We make two additional points: (1) in order to relate p as shown in Eq. (2) to the mean orientation of the GMF with respect to the POS (the angle γ), we need to assume that all parameters in Eqs. (A.1a)–(A.1c) are roughly uniform along the LOS; and (2) the total intensity in Eq. (A.1a) also depends on the GMF orientation through the angle γ. However, throughout our modelling procedure, we neglect this dependence.

In general the corrections to Stokes I caused by the GMF geometry are small, ranging roughly range between -7% and $+13\%$ for $p_0 \simeq 20\%$ (Planck Collaboration Int. XIX 2015). In our study, we focus on a region of the sky where the depolarization produced by $\cos^2 \gamma$ is small ($\cos^2 \gamma$ is mostly close to unity over the southern Galactic cap). Hence, in our study, the correction to Eq. (A.1a) would always be negative and less than 10%. Thus, in Sect. 5.3 we might estimate a value of p_0 slightly greater than the true value that we would have obtained by modelling the GMF correction for Stokes I. In practice Eq. (8) in Sect. 4.2 would change as follows:

$$Q_{353} = \frac{p_0 q_A}{1 - p_0 (\cos^2 \gamma - \frac{2}{3})} D_{353};$$

$$U_{353} = \frac{p_0 u_A}{1 - p_0 (\cos^2 \gamma - \frac{2}{3})} D_{353}. \tag{A.2}$$

The fits of steps A, B, and C would then not be linear in p_0 anymore, substantially complicating the fit. We argue that, considering the overall approximations (analytical and astrophysical) of our models, the GMF geometry in Stokes I is a minor issue.